nature sustainability

Article

https://doi.org/10.1038/s41893-024-01389-5

A bioinspired permeable junction approach for sustainable device microfabrication

Received: 14 September 2023

Accepted: 11 June 2024

Published online: 10 July 2024

Check for updates

Chuanwang Yang[1] ✉, Pengju Li[2], Chen Wei[3], Aleksander Prominski[1,4,5], Jingcheng Ma[1], Changxu Sun[2], Jiping Yue[4], Zhe Cheng[4], Jing Zhang[1], Brennan Ashwood[1,4,5], Wen Li[4], Jiuyun Shi[4], Kun Hou[1], Fengyuan Shi[6], Philip Griffin[2], Lihua Jin[3] ✉ & Bozhi Tian[1,4,5] ✉

Microfabrication, the process of fabricating small structures usually in micrometre scale, has wide practical applications but confronts sustainability challenges due to the substantial chemical and energy consumption during the patterning and transfer stages. Here we introduce a bioinspired permeable junction approach involving patterning on biopolymer matrices with a salt-assisted photochemical synthesis to advance sustainable microfabrication. This approach leverages an 'actuator-inhibitor-neutralizer' process for on-demand adhesion and delamination. Utilizing water as a green actuation agent, our method realizes instantaneous delamination (<1 s) for patterned device transfer, far exceeding the efficacy of traditional technologies. This advancement boosts the roll-to-roll production speed and minimizes the consumption of energy and hazardous chemicals. The combination of sustainable substrates and hazards-free processing substantially lowers greenhouse gas emissions and reduces environmental impacts for device fabrication compared with traditional microfabrication methods. This approach is widely applicable to various device fabrication processes, ranging from bioelectronic devices to catalytic robotics. Overall, this work addresses the sustainability challenges of microfabrication, paving the way to environmentally friendly device fabrication.

Microfabrication holds great promise for transforming sectors from healthcare to electronics[1,2]; however, it faces substantial environmental challenges, including high chemical usage, energy consumption and related greenhouse gas (GHG) emissions[3]. Microfabrication necessitates complex steps such as photolithography, deposition and transfer, which involve extensive use of hazardous chemicals such as etchants, organic solvents and fluorinated gases[4]. The industry's reliance on such chemicals results in nearly 1 billion cubic meters of etchants being consumed annually[5], with a projected global annual growth rate of 6.2%[6]. In addition, the dependence of microfabrication on non-renewable resource-based materials, from silicon or metal-based substrates to petroleum-derived polymers, magnifies its persistent environmental impact. Energy use is also a critical issue, with the semiconductor microfabrication industry alone accounting for ~1.5% of the industrial electricity usage in the United States[7,8]. Overall, the life cycle of microfabrication not only poses environmental burden

[1]The James Franck Institute, University of Chicago, Chicago, IL, USA. [2]Pritzker School of Molecular Engineering, University of Chicago, Chicago, IL, USA. [3]Department of Mechanical and Aerospace Engineering, University of California, Los Angeles, Los Angeles, CA, USA. [4]Department of Chemistry, University of Chicago, Chicago, IL, USA. [5]The Institute for Biophysical Dynamics, University of Chicago, Chicago, IL, USA. [6]Electron Microscopy Core, Research Resources Center, University of Illinois Chicago, Chicago, IL, USA. ✉e-mail: chuanwangyang@uchicago.edu; lihuajin@seas.ucla.edu; btian@uchicago.edu

in terms of hazardous chemical use but also intensifies global carbon footprints through energy-intensive procedures.

Application of green engineering principles to maximize mass, energy, space and time efficiency could potentially lead to notable environmental benefits for microfabrication. Conventional photolithography relies on photochemical reactions to pattern photoresist[4], which is resource-intensive both in terms of chemicals and energy. Reviving the subtractive processes through additive patterning could streamline fabrication procedures. Conventional patterning also requires a robust interfacial bond for adhesion, and hence involves the use of harsh chemicals or complex procedures during lift-off and transfer phases[9,10]. Striking a balance between strong adhesion for patterning and ease of delamination for transfer is crucial for developing sustainable and efficient microfabrication techniques[9,11]. Achieving this would eliminate the need for external etchants and allows for the reuse of preparation substrates, thereby minimizing waste. Interestingly, natural organisms exhibit on-demand adhesion and detachment behaviours through intricate junction structure. For example, locusts grow and shed protective exoskeletons during ecdysis through microvilli architecture (Fig. 1a, left)[12], geckos swiftly move on vertical walls through microscale junctions (Fig. 1a, middle)[13], and keratinocyte cells migrate across wounds through focal adhesion (Fig. 1a, right)[14]. These natural mechanisms utilize specialized tiny junction structures, categorized as either permeable or 'focal', for on-demand adhesion and detachment (Fig. 1b). Harnessing permeable junction strategy from natural systems may offer efficient pathways for material patterning and delaminating, thereby enhancing the sustainability of microfabrication methodologies.

In this work, we aim to develop a bioinspired permeable junction approach for sustainable microfabrication. We first proposed a salt-assisted photochemical process (Fig. 1b, right) for direct patterning of device on biopolymer substrates. We then constructed microscale junction structures with aerogel and cellulose paper, and utilized water to generate chemomechanical force for sustainable and efficient delamination[15]. The elimination of the use of hazardous chemicals and reduction in energy consumption make our method a universal platform for sustainable microfabrication. Given the eco-friendly and scalable advantages, our work holds promise for diverse device applications, including bioelectronics and robotics.

Results

On-demand pattern and delamination of device

We first demonstrate theoretically that when mechanical force prompts strain mismatches, permeable junctions resulted in fast delamination on the interface (Fig. 1c–e, and Supplementary Note 1, Figs. 1 and 2, and Video 1). Simulations using the cohesive zone model (Supplementary Note 1) reveal that permeable junctions greatly decrease delamination time from ~640 s (non-porous substrates) to ~2 s (Fig. 1e and Supplementary Video 2). This technique enables streamlined patterning (Fig. 1f–h) and transfer of device onto various surfaces, such as three dimensional (3D) objects, tapes and hydrogels for diverse applications (Fig. 1i,j and Supplementary Fig. 3).

Polymer-based substrates from renewable biomaterials can emulate the strain propagation of biological tissues for biomimetic patterning and delamination. We explored the potential of direct patterning and delamination of devices on natural polymer substrates, as illustrated in Fig. 2a. A well-established, CO_2 laser-based photochemical process was deployed for device patterning (Fig. 2a–c, details in Supplementary Note 2)[16]. However, the low char production of the biopolymer at high temperatures hinders graphitization[16]. To overcome this, we employed various salts for catalysing the photochemical synthesis, including $Na_2B_4O_7$, $MgCl_2$, $Fe(NO_3)_3$, $Co(NO_3)_2$ and $Zn(NO_3)_2$ (Supplementary Fig. 6). We utilized sodium borate as the catalyst to evaluate the synthesis conditions. The transient laser irradiation induces a localized temperature shock of 3,700 K at the focal point (Fig. 2b). The temperature acceleration averaged ~6.2×10^5 K s^{-1} under a critical laser energy of 11.2 mJ. The presence of sodium borate substantially enhanced the graphene yield under the ultra-high temperature condition (Supplementary Note 2)[17]. Raman spectroscopy confirmed the formation of graphene, indicated by distinctive peaks: the *G* peak (~1,580 cm^{-1}) and the 2D peak (~2,700 cm^{-1}) (Supplementary Fig. 6). Transmission electron microscopy (TEM) revealed an average lattice spacing of ~3.5 Å, indicating turbostratic graphene structures (Supplementary Fig. 8). This approach allowed the in situ formation of semi-crystalline carbon membranes on various hydrophilic scaffolds, such as sodium carboxymethyl cellulose (CMC), cellulose, sodium alginate and agar.

Drawing inspiration from natural systems, the application of chemomechanical forces is crucial for achieving efficient delamination on junction structures[18]. We assessed the hydration and swelling dynamics of cellulose paper (Fig. 2d and Supplementary Note 3) by altering intermolecular interactions among the anhydroglucose units within cellulose. We demonstrated two pathways to regulate cellulose fibre's swelling and mechanical properties, utilizing inhibitors (borate/M^{n+} ions), a neutralizer (ethylenediaminetetraacetic acid (EDTA)) and an activator (water). In the approach involving borate or $MgCl_2$, salt does not inhibit the swelling and water interferes with the 3-O···HO-6′ H-bond in cellulose II's amorphous zone, triggering rapid delamination without the need for energy/chemical-intensive etching processes (Extended Data Fig. 1 and Supplementary Video 1). Conversely, the M^{n+} pathway utilizes metal ions to chelate with hydroxyl groups, yielding a stable interfacial bonding. However, application of EDTA re-initiates hygroscopic swelling of cellulose and delamination in water (Supplementary Figs. 16–24)[15,19]. While the borate-based method is straightforward, the inhibitors offer chemical responsiveness for on-demand adhesion and delamination in microfabrication processes.

To identify the critical energy release rate, we performed a set of separation experiments in the borate pathway. Using different water:ethanol ratios to modulate the intermolecular H-bond (Fig. 2e and Supplementary Figs. 19–22), we successfully realized the control of the delamination process. Results show that the swelling ratio decreased proportionately with ethanol concentration, whereas delamination was inhibited at 75% ethanol ratio (Supplementary Fig. 19). The delamination threshold is met when the energy release rate (G) due to swelling surpasses the interfacial fracture energy between a membrane and a substrate (Γ_c), according to the equation:

$$G = \frac{1-\upsilon}{2(1+\upsilon)} LE\varepsilon^2 > \Gamma_c, \quad (1)$$

where L is the effective fibre thickness, υ is the Poisson's ratio of the fibres, E is the Young's modulus and ε is the swelling strain of cellulose fibres[20–22]. At 75% ethanol concentration, where $\upsilon = 0.3$, $L = 5$ µm, $E = 466$ MPa and $\varepsilon = 3.0\%$, the energy release rate is $G = 0.55$ J m^{-2}. At 0% ethanol concentration, where $E = 45$ MPa and $\varepsilon = 19.3\%$, the energy release rate is $G = 2.2$ J m^{-2}, which is ~3 times higher. Considering error bars, we estimate that the interfacial fracture energy is lower than the calculated energy release rates above, which is consistent with the values reported for thin film/substrate interface (~0.4 J m^{-2}) in the literature[22]. We also verified that water-induced instant separation is applicable to aerogel substrates with microscale junction interfaces (Supplementary Fig. 16).

Utilizing transition metal ions as inhibitors, cellulose fibres experienced effective swelling suppression and an increase in mechanical strength and stability (Fig. 2f)[15]. EDTA was used as a neutralizer to modulate the responsive behaviour of the junction. Upon immersion in a 0.1 M EDTA solution, the swelling ratio of metal-laden cellulose fibres increased markedly from under 5% to over 10%, boosting the energy release rate (~1.0 J m^{-2}) and triggering delamination (Supplementary Figs. 23 and 24). Past research indicates that capillary

https://doi.org/10.1038/s41893-024-01389-5

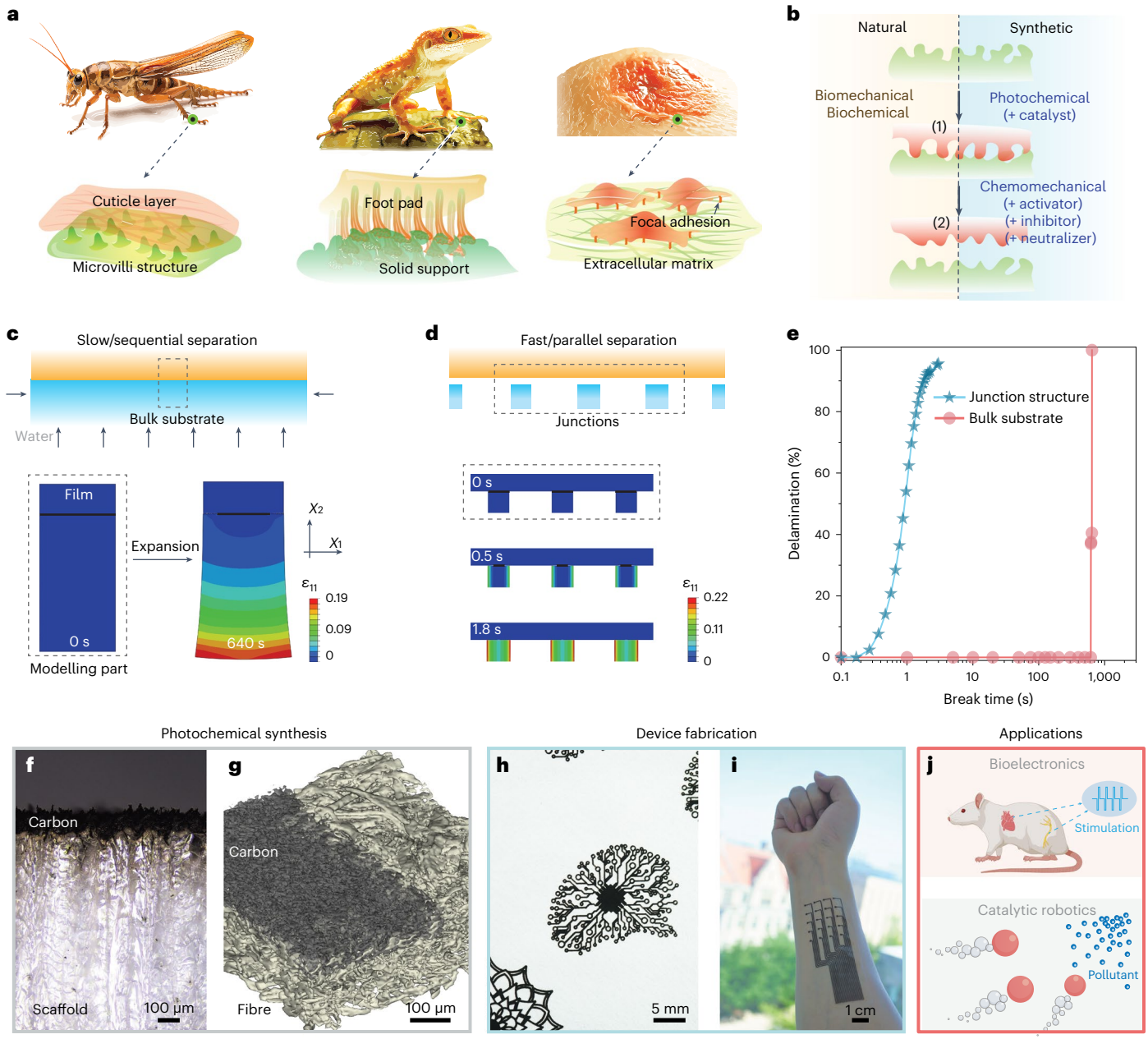

Fig. 1 | Bioinspired permeable junction strategy for sustainable microfabrication of carbon-based devices. a, Our delamination strategy is inspired by various microscale junction interfaces in natural systems, including exoskeleton ecdysis in locusts (left), instantaneous attachment and release of a gecko's footpad on the wall (middle), and keratinocyte migration on wound (right). **b**, Schematic diagram illustrating the responsive adhesion and delamination strategies of natural systems that employ biomechanical/biochemical mechanisms to drive sequential firm attachment (1) and on-demand release (2) at junction interface. Development of biomimetic synthetic materials that leverage both chemical and mechanical responsiveness on junction structures may present opportunities for enhancing adhesion strength while facilitating easy delamination for sustainable microfabrication. **c**,**d**, Simulations of interfacial delamination of a thin membrane from a planar bulk substrate (**c**) and a porous substrate with junction structures (**d**). Contour plots show the strain distributions in the horizontal direction. **e**, Delamination propagation dynamics show that the junction structure substantially expedites interfacial delamination by orders of magnitude in time under equivalent strain conditions. **f**, A cross-sectional image of a patterned carbon membrane atop a vertically oriented sodium carboxymethyl cellulose-based aerogel. **g**, Micro-computed tomography reconstruction of patterned carbon layer on fibrous cellulose network. Black, carbon; grey, cellulose microfibrils. **h**, Image of fabricated neuron- and flower-like devices on cellulose substrate. **i**, Photograph showing an EMG electrode array released from a porous cellulose substrate and attached to a human forearm through water-assisted tape transfer. **j**, Schematic illustrations showing the multifunctional applications of devices through sustainable microfabrication.

peeling arises from capillary forces when film–substrate adhesion is below the film–water tension[23]. Our measurements showed that the film–water interfacial tension (64 ± 3 mJ m^{-2}) is between the air–water (73 mJ m^{-2}) and graphene–water (17 mJ m^{-2}) tensions (Fig. 2g). The energy from cellulose swelling considerably exceeds surface tension energy, underscoring the pivotal role of junction swelling in delamination.

To elucidate the mechanism of instantaneous delamination, we crafted four substrates from sustainable materials with different porosities: (1) CMC film, (2) CMC aerogel, (3) cellulose paper and

https://doi.org/10.1038/s41893-024-01389-5

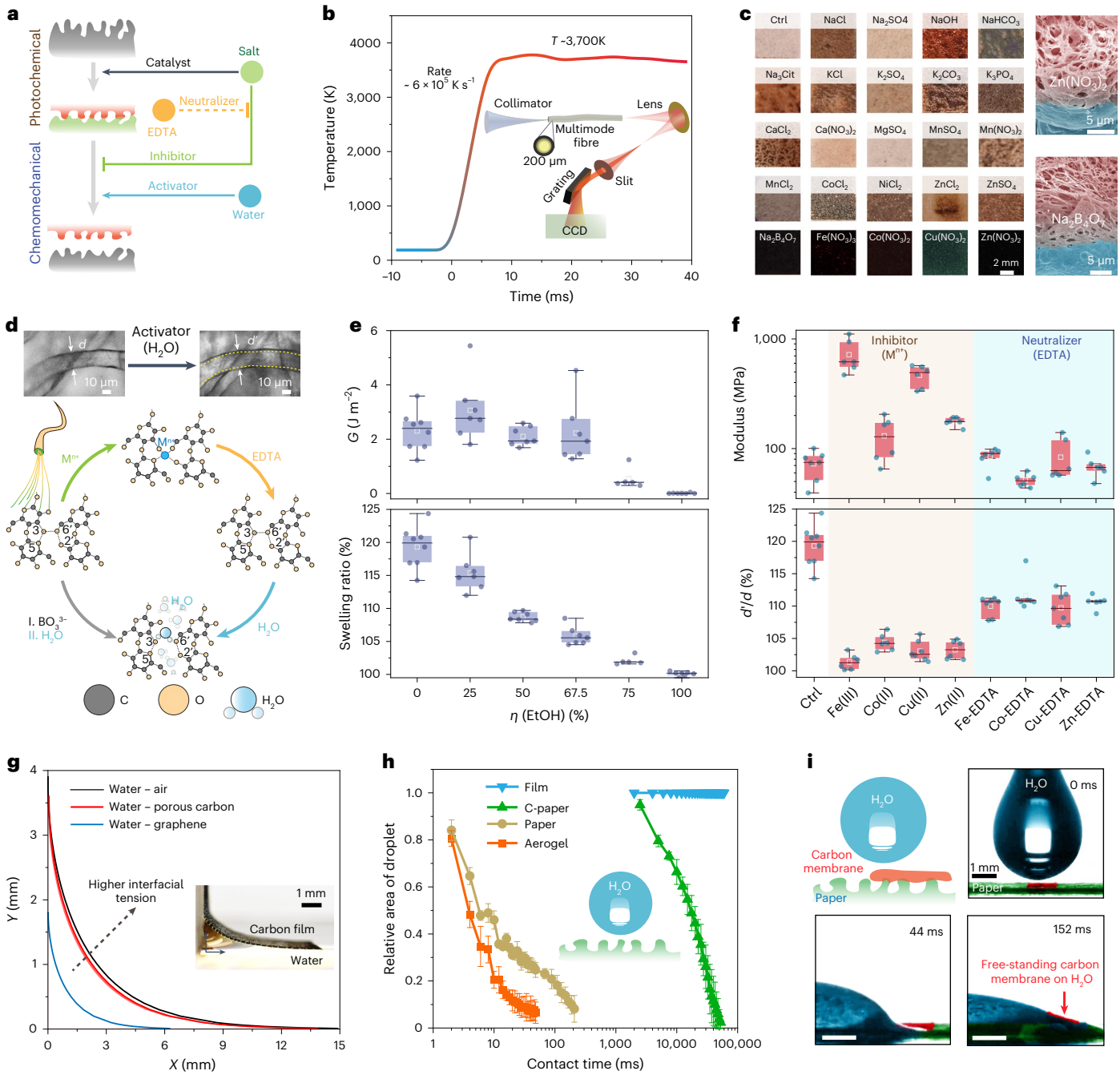

Fig. 2 | Salt-assisted laser patterning and instantaneous delamination of carbon device from permeable junctions. a, Schematic illustration of photochemical and chemomechanical processes of salt-catalysed laser patterning and water-activated delamination on junction interface. The chemomechanical force is generated using a chemical trio consisting of an activator (water), inhibitor (salt) and neutralizer (EDTA), with T-shaped and dashed lines representing each function. **b**, Profile of temperature increase during photochemical patterning. Inset: image illustrating the optical path for spectra collection. **c**, Optical images depicting carbon synthesis on paper substrates with/without salt catalysts, with pseudo-coloured scanning electron microscopic images on the right panel showing permeable junctions formed with the aid of $Zn(NO_3)_2$ or $Na_2B_4O_7$. **d**, Top: microscopic images of cellulose fibre before (left) and after (right) swelling in water, with dashed lines showing the original fibre position. Bottom: schematic illustration of borate- and M^{n+}-based routes for molecular-bond control over swelling and strength behaviours of cellulose fibre. **e**, Swelling index (d'/d) and the energy release rate (G) of cellulose fibres, which was controlled by modulating the intermolecular H-bond using ethanol:water mixtures. Boxplots represent the interquartile range (IQR) with the median line inside the box. Whiskers extend to ±1.5 times the IQR from the first and third quartiles. The mean value is shown by a white marker. All datapoints are plotted, with at least $N = 5$ independent samples. **f**, Change of Young's modulus (E) and d'/d of cellulose fibres in the presence of various inhibitors (M^{n+}) and a neutralizer (EDTA). Boxplots represent the IQR with the median line inside the box. Whiskers extend to ±1.5 times the IQR, with the mean value shown by a white marker inside the box. All datapoints are plotted, with at least $N = 6$ independent samples. **g**, Measurement of the interfacial tension between water and the free-standing carbon film with comparisons of theoretical values of the water–air interface and water–dense graphene interface. Inset: image showing the cross-section of the water meniscus formed between the delaminated carbon membrane and the cellulose substrate. **h**, Penetration dynamics of water droplets represented by the change in relative droplet area over contact time. Data were analysed from $N = 3$ independent experiments, with results expressed as mean ± s.d. **i**, Schematic and image sequence of water-assisted separation of thin carbon layer from porous cellulose substrate.

(4) compressed cellulose paper (Supplementary Fig. 26). Using a sandwich test, we assessed the interfacial fracture energy between substrates and adhesive tape, revealing that higher porosity diminished peel adhesion strength. The fracture energy decreased from 145.6 J m^{-2} (CMC film) to 15.6 J m^{-2} (CMC aerogel) and 86.9 J m^{-2} (compressed paper) to 69.4 J m^{-2} (cellulose paper) (Supplementary Fig. 27). High-speed imaging (Fig. 2h and Supplementary Fig. 28) verified enhanced water droplet penetration in porous substrates, which substantially amplifies swelling dynamics. Subsequent delamination observations revealed rapid water-induced swelling and membrane detachment within ~152 ms (Fig. 2i), over three orders of magnitude faster than current etching/electrochemical/dry delamination methods used to delaminate the graphene layer from Cu foil (Extended Data Fig. 1, and Supplementary Video 1 and Table 6)[24–29]. In comparison to natural hygroscopic actuators such as silk, seeds and mimosa, our junction-driven actuation achieves reduced delamination periods (~150 ms in water to ~250 ms in 50% ethanol) at comparable stress levels (~10^7 Pa) (Supplementary Fig. 29). In addition, a paper substrate also offers support for thermoforming in additive manufacturing, enabling the fabrication of thin-layered 3D patterns upon wet release (Supplementary Figs. 4 and 5). The 'permeable junction' strategy also proves to be a universal approach for microfabrication on rigid substrates (for example, silicon wafers, glass), with cellulose nanofiber (CNF) notably enhancing delamination efficiency. Our findings show that CNF enables rapid delamination of Au-based bioelectronics created via traditional photolithography or thermoplastic-based objects via the additive manufacturing process (Extended Data Fig. 2 and Supplementary Figs. 30–33). This nanojunction strategy presents unparalleled efficiency over traditional methods for fabricating multifunctional devices with enhanced precision.

A versatile platform for device microfabrication

Our method enables the versatile tuning of patterning and material property (Fig. 3a,b). We achieved a line width of 90.1 µm on cellulose paper (Supplementary Fig. 34), with the potential to reach resolutions finer than 50 µm[30]. This method proved to be compatible with a variety of metal salts across different concentrations. Taking platinum (Pt) as an example, we achieved single-atom dispersion of Pt to nanoparticle encapsulation in semi-crystalline carbon matrix (Fig. 3a, and Supplementary Figs. 35 and 36). At a low precursor concentration (K_2PtCl_4, 0.025 wt% in 0.15 M sodium borate solution), single Pt atoms are dispersed. In contrast, a higher concentration (5%) leads to the encapsulation of Pt nanoparticles with an average size of 23.1 nm. This reduction behaviour of carbon at high temperatures is consistent with the Ellingham diagram[31]. Using laser additive manufacturing, various metals or carbide nanoparticles (Mn, Fe, Co, Ni, Cu, Pd, TiC, WC/W_2C and Mo_2C, Fig. 3b) can be integrated into carbon matrices (Supplementary Figs. 37–39). The carbon membrane can also serve as a template for silicon growth, enabling porous semiconductor production (Supplementary Fig. 40). This versatility underscores the potential of our method for generating materials with tailored properties for specific applications.

We employed three eco-friendly water-assisted transfer techniques, circumventing pollution from the traditional etching process[9–11]. Water-phase transfer capitalized on capillary forces (Fig. 3c and Supplementary Fig. 3), while hydrogel-based transfer used the water content in polyacrylamide hydrogels (>90 wt%) for delamination and transfer. In addition, water-assisted tape transfer achieved direct pattern transfers onto adhesive substrates. Compared with other laser-based fabrication methods[16,32,33], our permeable junction strategy enables efficient device transfers from the original substrate to a variety of others, spanning from non-adhesive 2D surfaces to complex 3D structures (Supplementary Table 7).

Our nature-inspired approach of permeable junction formation supports sustainable on-demand, renewable attachment and delamination. As a demonstration, we patterned a serpentine image, transferred it to transparent tape and regenerated the porous substrate post transfer (Supplementary Figs. 41 and 42). This allowed stepwise patterning, such as a house followed by the diagrams of industrial smokestacks and an electroencephalography experiment, on the same substrate, demonstrating the repeatability of the process from the same initial substrate (Fig. 3d). The distinctive properties of porous carbon materials, including high surface area, electrical conductivity and flexibility, provide a versatile platform for diverse applications in fields such as supercapacitors, sensors and flexible electronics (Supplementary Figs. 43–45).

Fabrication of flexible bioelectronics

To showcase potential applications, we first established a platform for bioelectronics fabrication. This involves the development of microcapacitors and the construction of effective biointerfaces for electrical modulation or sensing of neural and cardiac systems (Fig. 4a)[10].

For neural modulation, we developed cuff-type neural electrodes through water transfer of carbon-based electrodes onto thin polyethylene terephthalate (PET) films (thickness, 12.5 µm) (Fig. 4b and Supplementary Fig. 46). The compliant carbon electrodes formed a seamless interface with soft sciatic nerve of rat, facilitating electrical coupling. We electrically stimulated the sciatic nerve using a traditional Au electrode and the carbon electrode, and recorded action potentials from the muscles[34]. We observed clear limb movement synchronized with each current injection (Supplementary Video 3), which was corroborated by electromyography (EMG) recordings from the rat limb. EMG results displayed large potential spikes in synchrony with the cathodic phase (Fig. 4c, and Supplementary Figs. 47 and 48). The carbon electrodes exhibited neuromodulation capabilities analogous to those of the traditional Au electrode, demonstrating their potential as soft and flexible neural stimulators.

Nanostructured carbon materials present an effective solution to enhance bioelectronic device performance owing to their high charge storage capacity[35]. Traditional methods for creating carbon-based electrodes include electrodeposition, spin coating and screen printing, which are limited by patterning capabilities or complex precursor preparation procedures[36]. Relatively, our method enables facile patterning and instant transfer of carbon device onto traditional Au electrodes for enhancing performance (Fig. 4d and Supplementary Figs. 49–51). The Helmholtz capacitance of the Au electrode increased significantly after carbon coating, from 0.025 to 1.98 mF cm^{-2} (Supplementary Fig. 43). The increase in capacitance using this microcapacitor coating strategy can effectively lower the polarization voltage. Impedance characterization further confirmed that the carbon coating substantially reduced the impedance of the Au electrode by roughly two orders of magnitude, from 7,244.4 to 63.1 Ω at 100 Hz frequency pertinent to electrocardiogram (ECG) signals (Fig. 4e). We then evaluated the efficiency for cardiac stimulation. Using a Langendorff perfusion system, the Au or Au-C electrode was placed on the left ventricular wall for charge injection at biphasic square current waveforms (Fig. 4f–h). Upon 4 Hz stimulation (1 mA), both Au and Au-C electrodes achieved effective overdrive pacing (Supplementary Video 3). However, a notably higher ECG amplitude, indicative of contraction strength, was observed in the Au-C group. Both electrodes demonstrated an exponential decrease in the threshold current for stimulation with pulse duration. The strength–duration curve was modelled using the equation: $I(t) = I_{rheobase}/(1-\exp(-t/\tau))$, where $I(t)$ refers to the stimulus current at the pulse duration (t), $I_{rheobase}$ is the threshold current at an infinitely long pulse duration (rheobase) and τ is the membrane time constant[37]. We calculated the minimum charge necessary for successful stimulation at chronaxie as $Q = I_{rheobase} \times \tau$. Q_{min} values were determined as 0.79 and 0.71 µC for Au and Au-C electrodes, respectively (Fig. 4g). Stimulation thresholds, which indicate the lowest voltages for effective frequency modulation, were also measured across various

https://doi.org/10.1038/s41893-024-01389-5

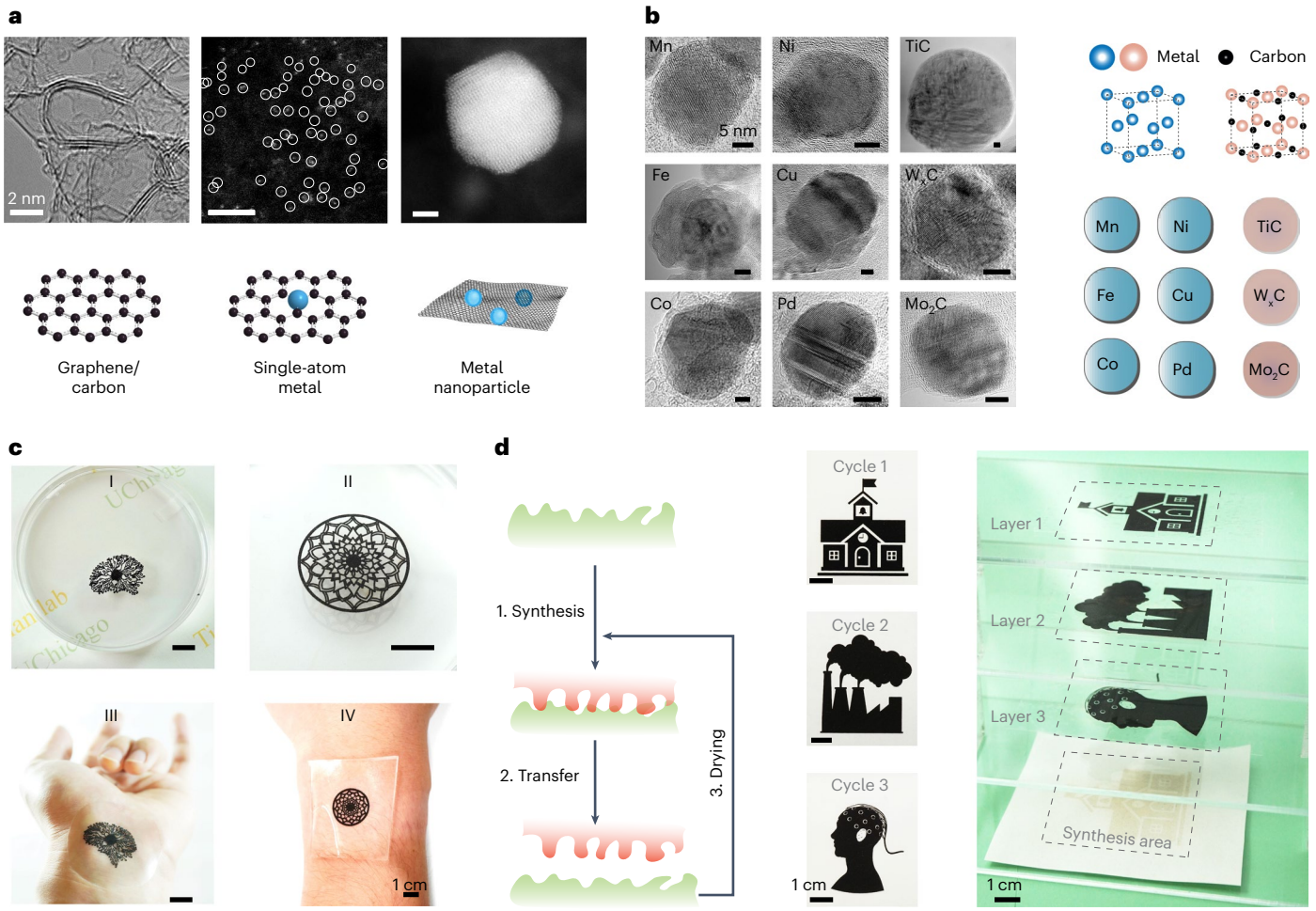

Fig. 3 | Eco-friendly and versatile fabrication of multifunctional devices. **a**, STEM images and illustrations of semi-crystalline carbon (left) and encapsulation of well-dispersed Pt atoms (middle) and Pt nanoparticles (right) within carbon shells. **b**, TEM images of metal (Mn/Fe/Co/Ni/Cu/Pd) and metal carbides (TiC/W_xC/Mo_2C) incorporated within the carbon device. **c**, Water-assisted transfer of carbon device onto various substrates, including water-phase separation on water surface (I–II), transfer to tape (III) and hydrogels (IV). **d**, Schematic illustration and optical images of repetitive pattern transfer from the same substrate through permeable junction design. The three printed layers depict the transferred house, industrial smokestacks and an electroencephalography experiment onto three transparent PET/acrylic plates.

pulse widths (Fig. 4h). At a stimulation current of 4 mA cm^{-2}, threshold voltages for effective stimulation were observed at 1.32 V and 0.90 V for Au and Au-C electrodes, respectively. The 30.3% reduction in threshold voltage suggests a potential decrease in oxidative stress during prolonged stimulation[35], thus facilitating safer bioelectronics application with minimal tissue damage. In addition, we developed a carbon-grafted 16-channel Au electrode for enhanced epicardial ECG signal detection (Fig. 4i and Supplementary Fig. 52). The nanostructured carbon transfer notably improved the signal-to-noise ratio by 8.0-fold compared with traditional Au electrodes (Supplementary Fig. 53), demonstrating the effectiveness of our approach for high-fidelity bioelectronics.

Fabrication of catalytic robotic devices

The release of heavy metals and organic pollutants into the environment due to human activities poses important sustainability challenges, which requires the development of advanced sensing and remediation devices. To address these issues, we introduce a sustainable microfabrication method for robotic devices. Such robotic device is inspired by waterborne insects such as water striders, which demonstrate active movement and responsiveness to environmental cues such as threats or food sources (Fig. 5a). We engineered a robot with a carbon pattern incorporating Pt and transferred it onto a thin, hydrophobic PET film. This robotic device propels itself by harnessing chemical energy through the Pt-catalysed decomposition of H_2O_2 into O_2, simulating the dynamic movement of water striders (Fig. 5b,c). The propulsion mechanism during burst dynamics of O_2 bubbles involves phases of liquid film retraction and fragmentation (0 ms), cavity collapse (10 ms), jet formation and breakup (20 ms), and robot propulsion in the opposite direction (80 ms). Using a machine learning algorithm (DeepLabCut)[38], we established an automated trajectory analysis workflow (Fig. 5d) encompassing video capture, labelling and network training (Supplementary Video 4). We optimized catalase-like performance by altering the precursor concentration of Pt and pH during device fabrication, achieving an H_2O_2 (20 mM) decomposition rate of 5 mmol l^{-1} min^{-1} cm^{-2} (Supplementary Figs. 54 and 55). Microscopic observations of bubbles on Pt-carbon particles showed a bubble growth function of $R \propto t^{1/2}$ with a minimum growth constant of 17.2 µm (Fig. 5e and Supplementary Fig. 56). After nucleation, bubbles grew and coalesced on catalytic film, promoting the continuous swimming of the robot (F_{growth}, Fig. 5f). Upon reaching maximum size, bubbles burst, releasing high-pressure O_2 gas and inducing a jumping motion (F_{burst}). The random walking and jumping behaviour of the bioinspired robots was found to be size dependent and shape independent (Supplementary Figs. 57–59). The highest velocity (~2.7 mm s^{-1}) was observed in robots with 8 mm diameter (Supplementary Fig. 59). The catalytic robots maintained their

https://doi.org/10.1038/s41893-024-01389-5

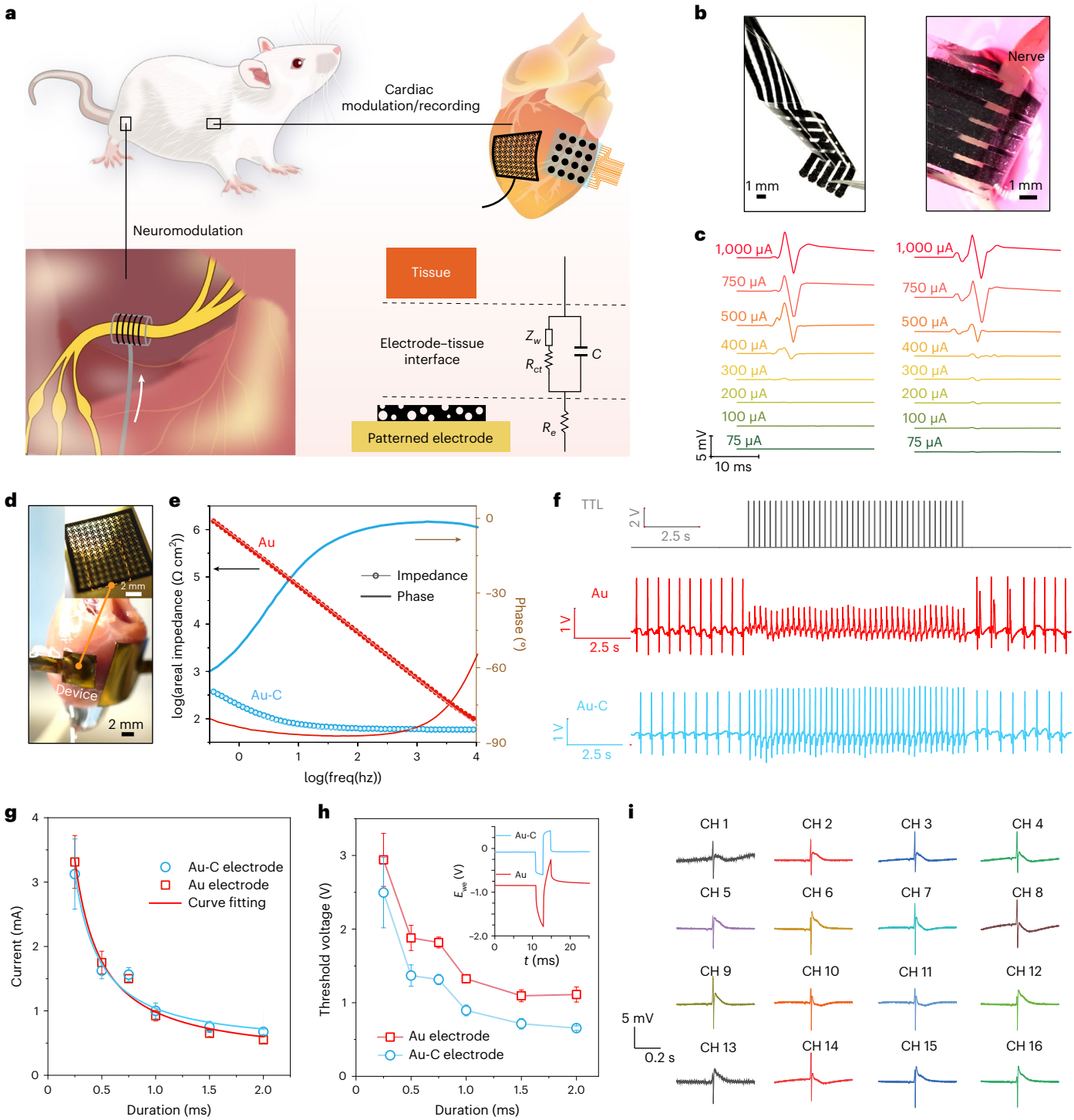

Fig. 4 | Sustainable microfabrication for device patterning and transfer for flexible bioelectronics. a, Schematic illustration depicting transfer of porous carbon patterns onto flexible substrates for application in sciatic stimulation, low-voltage heart stimulation and high-fidelity ECG recording. The lower right panel shows the electrochemical interface between excitable tissues and patterned carbon interfaces. **b**, Image of fabricated soft carbon electrode on a thin PET film (left) and the wrapped sciatic nerve within the carbon electrode (right), showing a compliant interface. **c**, EMG response of skeletal muscle under different stimulation currents (from 75 to 1,000 μA) using Au (left) or carbon electrode (right) at a frequency of 4 Hz. **d**, Optical image of a porous carbon membrane-grafted Au (Au-C) electrode for heart stimulation. Inset: image showing the enlarged view of a serpentine-structured microcapacitor on the Au electrode. **e**, Impedance and phase spectra of Au and Au-C electrodes with fitted curves according to the circuit displayed in **a**. **f**, ECG response of isolated rat heart to biphasic, square current waveform stimulation at a frequency of 4 Hz. Under the same current density of 4.0 mA cm^{-2}, the heart showed different ECG responses under stimulation from Au or Au-C electrodes. **g**, Duration–strength curves of Au and Au-C stimulation electrodes and their curve fitting are present at a stimulation frequency of 4 Hz. **h**, Threshold voltage for stimulation at different durations for Au and Au-C electrodes. Inset: figure showing representative voltage change during a biphasic stimulation cycle. Threshold current and voltage were recorded from $N = 6$ stimulation replications for $N = 4$ independent devices. Results are presented as mean ± s.d. **i**, Representative ECG traces obtained from the 16-channel, carbon-coated recording electrode display the spatial rat epicardial electrical activities.

https://doi.org/10.1038/s41893-024-01389-5

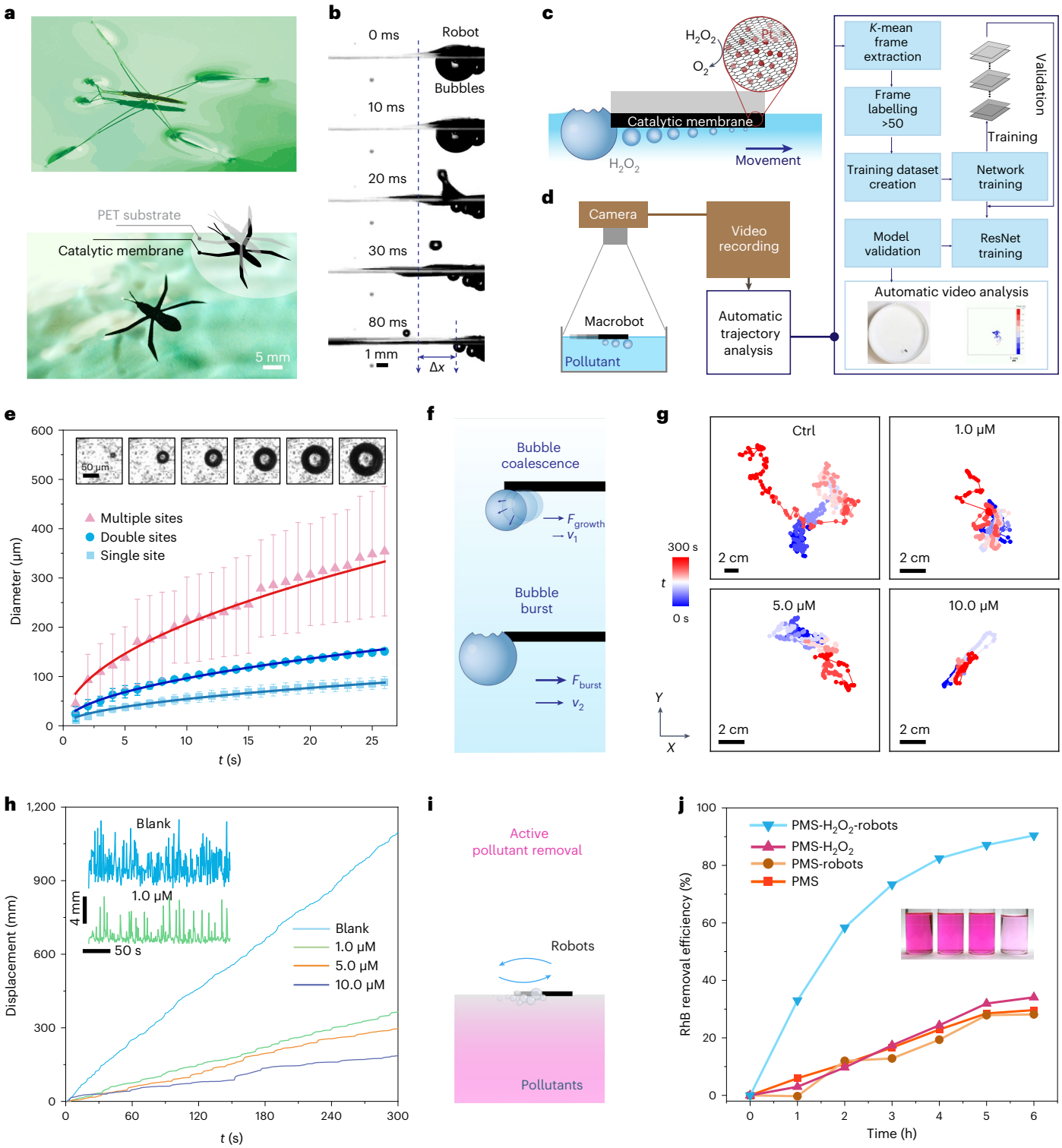

Fig. 5 | Sustainable microfabrication of catalytic device for robotic sensing and environmental remediation. a, Top: schematic illustration of a water strider swimming on a water surface. Bottom: an optical image of a biomimetic nanozyme-powered soft robot transferred on PET film. The schematic on the top-right of the bottom panel shows the layered structure of a catalytic membrane. **b**, High-speed images demonstrate the burst dynamics of a single bubble at the edge of robots. After creating an air cavity in the margin of the robot, a water jet forms and creates a water wave, which propels the robot's movement (Δx) in 80 ms. **c**, Schematic illustration of the motion of biomimetic robots, which is fuelled by O_2 bubbles generated via catalysis of H_2O_2 through the embedded Pt nanoparticles. **d**, Workflow diagram for extracting the trajectories of robots for automatic behaviour analysis. **e**, Diameter change of O_2 bubbles on single, double and multiple sites of Pt-embedded carbon particles. Inset: optical images of growing bubbles on an individual particle. Data were analysed from $N = 3$ independent experiments and the results are expressed as mean ± s.d. **f**, Schematic of the generated coalescence force (F_{growth}) and bubble burst force (F_{burst}) during O_2 generation. **g**, Trajectory analysis of a catalytic robot with nanozyme-powered motion in 1.0 M H_2O_2 solution, and biomimetic robotic sensing of Hg(II) at different exposure concentrations. **h**, Displacement of the robots after exposure to varying Hg(II) concentrations. Inset: jumping analysis. **i**, Schematic of active pollutant removal using swimming robots with external energy input. **j**, Time-dependent removal efficiency of RhB pollutant under various treatment conditions. Inset: photo showing the RhB colour change in different groups.

https://doi.org/10.1038/s41893-024-01389-5

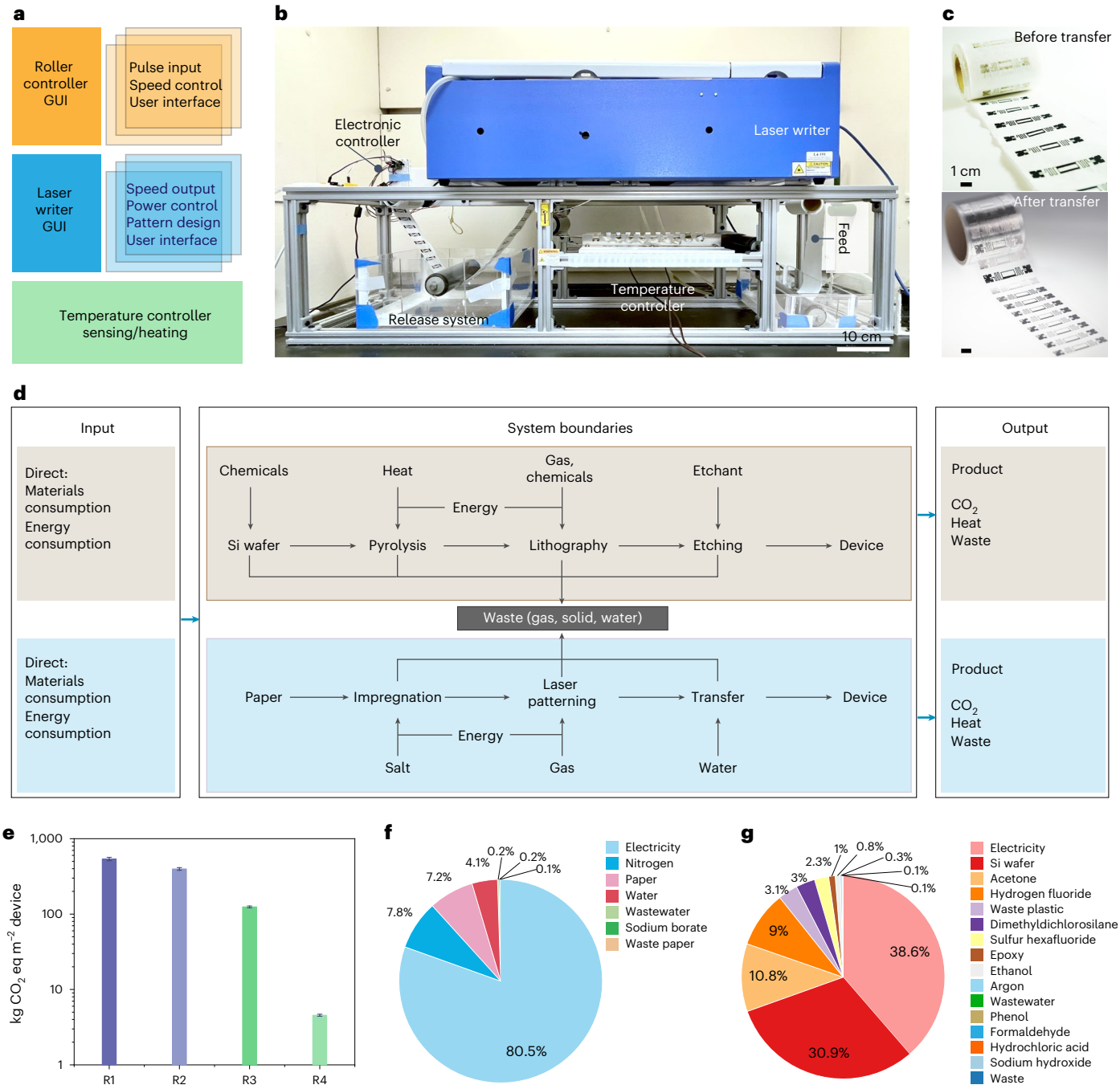

Fig. 6 | Scalable microfabrication with minor environmental impact. **a**,**b**, System design (**a**) and image (**b**) of the home-built R2R apparatus, showcasing electrical components and fabrication systems, such as roller controller and laser writer graphical user interfaces (GUI), paper feed, salt-impregnation system, laser scanner, roller system, electronic controller and product collector. **c**, Optical images of fabricated RFID patterns on a paper roll and the transferred patterns on a PET roll. **d**, Top: the system boundaries of conventional microfabrication method based on pyrolysis + lithography techniques. Bottom: our approach for device fabrication. **e**, Comparative analysis of GHG emissions for producing a 1 m^2 device (measured in kg CO_2 equivalent) using different fabrication methods: the pyrolysis + lithography route (R1), CVD + lithography route (R2), lasering + casting route (R3) and the route proposed in this study (R4). Data distribution, presented as mean ± s.d., is derived from 1,000 trials of Monte Carlo simulation within the 95% confidence interval. **f**,**g**, Analysis of GHG emission contributions by factors in R4 (**f**) and R1 (**g**). Each pie chart in this figure displays the distribution of different contributing factors, either materials, energy or waste, to the total GHG for each fabrication route.

jumping behaviours for weeks due to the protective carbon shells around the Pt nanoparticles, which indicates their potential for long-term environmental monitoring and pollutant remediation applications.

The discharge of heavy metals, notably Hg(II), from industrial processes into the environment poses notable environmental and health risks. We explored the potential of the bioinspired robot for Hg(II) tests (Fig. 5g,h) by observing its movement behaviour when exposed to Hg(II). In an unpolluted environment, the robot exhibited a jumping frequency of 15.2 jumps per minute and an average velocity of 3.7 mm s^{-1} in H_2O_2 solution. However, exposure to a 1 μM concentration of Hg(II) markedly reduced its mobility, leading to a decreased jumping

frequency of 3.4 jumps per minute and an average velocity of 1.1 mm s^{-1}. Higher concentrations of Hg(II) further suppressed jumping frequency and velocity (Supplementary Fig. 61). This method shows the potential to detect Hg(II) at concentrations as low as ~500 nM. Compared with conventional, sophisticated analytical instruments, our robotic sensor uses only a handheld camera for monitoring, offering a practical and versatile approach for on-site water quality monitoring in rural areas.

To mitigate environmental pollution caused by organic compounds, nanozyme-powered robots offer an environmentally friendly solution for active abatement of pollutants (Fig. 5i,j)[39]. Using rhodamine B (RhB) as a test pollutant, we measured RhB removal efficiency over time with four systems: (1) the pollutant remediator peroxymonosulfate (PMS), (2) PMS + nanozyme-powered robots, (3) PMS + H_2O_2 and (4) PMS + H_2O_2 + robots. The inclusion of robots, especially when integrated with H_2O_2 as an external energy source, substantially accelerated the pollutant removal process. The active motion enables active pollutant adsorption and degradation with the synergistically catalytic effect from carbon and PMS. The robots function as autonomous cleaners, exhibiting efficient (94%) removal of organic dye within 6 h (Fig. 5j and Supplementary Fig. 62). Compared with previous micro-sized particulate robots[40–42], our design of 'floating' macro-sized robots facilitates observation, recycling and reuse for environmental remediation.

Scalability and sustainability evaluation

To illustrate the scalability of our approach, we built a roll-to-roll (R2R) apparatus for the automated production of carbon-based devices. The R2R apparatus incorporates an integrated system including a salt-impregnation unit, an electronic roller module, a laser writer and the water-assisted transfer system (Fig. 6a,b, Extended Data Fig. 3, and Supplementary Fig. 63 and Video 5). Employing a commercial paper roll, the R2R apparatus realized continuous fabrication for radio frequency identification (RFID) pattern (5.0 cm × 0.8 cm) at a rate of 800 mm h^{-1} (Fig. 6c). The RFID tags can be swiftly transferred onto transparent PET rolls through a water-assisted process. An economic assessment of the materials and manufacturing process reveals that our technique is economically feasible, with an overall production cost estimated at ~US$1 per square metre. This cost efficiency is primarily due to the streamlined patterning and transfer processes with minimal use of chemicals and energy.

Compared with the subtractive processes typically used in conventional microfabrication, our research introduces an additive patterning approach. This approach replaces traditional processes such as photolithography and etching, and therefore reduces material and energy demands. To evaluate the environmental impact of our method, we conducted a preliminary life cycle analysis (LCA) during the 'cradle-to-gate' stage on the basis of the input of material and energy and the output of waste. Comparative analysis was conducted against conventional methods for fabricating carbon-based devices, including chemical vapor deposition (CVD) + lithography methods[43], pyrolysis + lithography method[10] and lasering + casting method[30] (Fig. 6d, Extended Data Figs. 4 and 5, and Supplementary Fig. 64 and Tables 8–12). The LCA result indicates that the GHG emissions for device fabrication per functional unit (m^2 device) by our proposed method are significantly lower (4.56 kg CO_2 eq) compared with pyrolysis (537.04 kg CO_2 eq), CVD (397.47 kg CO_2 eq) and lasering (124.55 kg CO_2 eq) methods, within a 95% confidence interval (Fig. 6e). In our method, the primary sources of GHG emissions are energy consumption, contributing 3.67 kg CO_2 eq m^{-2} device, and gas usage, adding 0.36 kg CO_2 eq m^{-2} device (Fig. 6f). By utilizing sustainable paper substrates and streamlining the fabrication and delamination processes, we substaintially lower the carbon footprint. Moreover, our method shows the least environmental impact in terms of resource consumption, effects on terrestrial ecosystems, acidification and human health (Extended Data Fig. 5). In contrast, conventional methods involve intense consumption of materials and chemicals such as Si wafers, epoxy, photoresist, etchants, organic solvents and electricity consumption, which result in substantially higher environmental impacts (Fig. 6g).

Discussion

Microfabrication techniques, essential for electronics, healthcare, robotics and other sectors, face inherent environmental challenges. We try to address this issue with a bioinspired strain engineering approach at permeable junctions, which resolves the duelling requirements of firm attachment and rapid release during microfabrication, thereby reducing energy and chemical consumption. While this approach primarily targets the production of carbon-based bioelectronic and catalytic devices, it holds the potential to serve as a model for making microfabrication techniques across various materials and device systems more sustainable. Demonstrating this, the CNF-enabled 'permeable nanojunction' strategy achieves highest efficiency in fabricating bioelectronic devices compared with traditional methods. This universality highlights the potential of our platform for generating devices with tailored properties for specific applications.

As we look to the future, manufacturing is moving towards being large scale, intelligent and carbon neutral. Our work demonstrates the practicality of continuous roll-to-roll processes to scale up from small laboratory experiments to large manufacturing production. The shift from traditional batch processing to automated manufacturing and even data-driven online monitoring represents the manufacturing nexus. Concurrently, the manufacturing sector must prioritize minimizing the carbon footprint throughout the life cycle. We introduce LCA in our work to preliminarily quantify the environmental footprint of representative systems. In the future, by incorporating advanced analytical tools from the data science field, the flows of material, energy and greenhouse gases can be digitalized to comprehensively assess the environmental impacts of various microfabrication techniques across different stages. Identifying carbon emission hotspots will facilitate the development of effective solutions toward sustainable commercialization and application. As a starting point, our paradigm holds potential for guiding carbon-neutral development across many sectors, including energy storage devices, sensors, flexible electronics and robotics, and so on.

Methods

Substrate fabrication

To prepare porous substrates, aqueous suspensions of sodium alginate (alginic acid sodium salt from brown algae, Sigma), CMC (average Mw ~250,000, Sigma) and agar (Fisher) were first prepared by autoclaving under 100 °C for 15 min. Suspensions with weight concentrations between 5% and 10% (w/v) were then poured into plastic moulds to achieve thicknesses ranging from 1 mm to 4 cm. Subsequently, the suspensions or gels underwent directional freezing in a dry ice and ethanol cooling bath at −72 °C. After complete freezing, samples were freeze dried for 3 days under 0.03 mbar pressure using a freeze dryer (Labconco) to form layer-structured porous scaffolds. Polymer membranes were created by pouring polymer suspensions into moulds and vacuum drying for 4 days at 60 °C.

Common fibre-based porous substrates utilized were a selection of Whatman filter papers, including Grade 1, 602H and 595 (Sigma). For the preparation of compressed paper substrates, Grade 1 Whatman filter papers were moistened with H_2O and placed between two stainless steel plates. The assembly was then subjected to a platen press (Dake, 44-225) at ~6 metric tons (~5 MPa) of pressure and heated to 100 °C overnight.

Substrates preparation for photochemical synthesis

The fabrication of carbon membranes was accomplished using a salt-impregnation method. For fabrication on various aerogel samples, suspensions of different precursors were prepared in sodium borate solutions (0.15 M, pH 9.4) and freeze dried. Grade 1 Whatman

filter paper primarily served as the representative fibre-based porous substrate. The paper was first impregnated in aqueous solutions of sodium borate (0.15 M, pH 9.4), $MgCl_2$ (0.5 M), $Fe(NO_3)_3$ (0.5 M), $Co(NO_3)_2$ (0.5 M) and $Zn(NO_3)_2$ (0.5 M) for 1 h and then dried at 60 °C overnight. Laser synthesis was performed using a CO_2 laser (VLS 4.60, Universal Laser Systems) with pre-designed patterns. Patterning was conducted in raster mode with optimized parameters (power, 1.8 W; speed, 1.6 cm s^{-1}; points per inch, 1,000).

To fabricate metal-incorporated membranes, metal salts were either dissolved in water (0.5 M) or in sodium borate solution (0.15 M, pH 5.0). Paper substrates were impregnated in the mixed salt solution for 1 h and then dried at 60 °C overnight. Laser fabrication and water-phase transfer were conducted.

Swelling analysis and water-assisted transfer

The fibre network structures of cellulose-based substrates were examined using an inverted microscope (ECLIPSE Ti-2, Nikon). Structure profiles of cellulose fibres from various substrates, both before and after wetting, were analysed with ImageJ (Fiji, v.1.53t). The swelling index (d'/d) and the energy release rate (G) of cellulose fibres were modulated by adjusting the intermolecular hydrogen bonds using ethanol:water mixtures. Sample sizes were $N = 8$ for the 0% ethanol group, $N = 7$ for the 25, 50 and 100% ethanol groups, and $N = 5$ for the 75% ethanol group. The inhibitory effect of metal ions and the neutralization effect of EDTA were also investigated. Post-treated cellulose substrates were immersed in a 0.1 M EDTA solution, and the swelling ratios were measured. Sample sizes were as follows: $N = 8$ for Ctrl, $N = 6$ for Fe(III), $N = 6$ for Co(II), $N = 7$ for Cu(II), $N = 6$ for Zn(II), $N = 7$ for Fe-EDTA, $N = 6$ for Co-EDTA, $N = 7$ for Cu-EDTA and $N = 6$ for Zn-EDTA.

Water-assisted transfer was conducted via two processes: water-phase separation and capillary transfer (Supplementary Fig. 3). In the water-phase separation experiment, paper substrates were wetted with water. The swelling strain facilitated the separation of the carbon membrane from the supporting substrate in less than a second, causing it to float on the water surface. In a capillary transfer experiment, the supporting substrate was initially submerged in water and brought into contact with one end of the desired carbon membrane to form a contact line (the transfer front). For hydrophobic supporting substrates, external force could be applied to assist in forming the contact line. Then, the substrate was held by hand or a rotary knob and moved in a tilted or vertical direction at a low velocity. The high flexibility of the carbon membrane allowed it to conform to rough or 3D surfaces, enabling further fabrication on 3D devices or tissues.

Nanofibre-accelerated microfabrication

TEMPO oxidation for CNF synthesis (Supplementary Fig. 30)[44]: This process is initiated with the mechanical crushing of cellulose paper (Whatman, Grade 1) using a kitchen blender. The cellulose slurry then undergoes an alkaline-acid pretreatment, where it is soaked and stirred in a 15 wt% solution of NaOH for 2 h. The fibres are then collected and subjected to thorough washing with distilled water. The microfibres are further processed through hydrolysis using a 1.0 M solution of HCl at 80 °C, again for 2 h, facilitating the solubilization of hemicelluloses. After centrifugation and washing, the fibres are bleached with a 2.0 wt% NaOH solution at 80 °C for 2 h. After centrifugation and washing, the pulp is suspended in deionized water (~2.0 wt%) and vigorously stirred. An aqueous solution containing sodium bromide (750 mg) and TEMPO (90 mg) is added and the mixture is stirred continuously for 10 min. Next, a 4% sodium hypochlorite solution (30 ml) is added dropwise while maintaining the pH between 10 and 11 by adding sodium hydroxide. This mixture is left to react for 12 h, following rinsing with water. Finally, the TEMPO-oxidized pulp slurry is agitated using a kitchen blender for 5 min to yield a CNF dispersion.

CNF-enabled microfabrication and additive manufacturing (Supplementary Figs. 31–33): Adhesion layer solutions are prepared by dissolving various polymers (CMC, dextran and CNF) in water to achieve concentrations ranging from 2 to 5 wt% and then filtered (size cut-off: 0.22 µm). Rigid substrates such as silicon wafers (prime grade, 4-inch, Nova Electronic Materials) and glass slides are cleaned with acetone and isopropanol. These substrates are then treated with a 200 W oxygen plasma for 25 s and subsequently spin coated with the prepared adhesion layer solutions at 1,500 r.p.m., followed by a drying phase at 90 °C for 30 min. In the fabrication of flexible electronics, an SU-8 layer (SU-8 3005, Kayaku Advanced Materials) of ~8 µm thickness is spin coated, baked (95 °C, 15 min), patterned using direct writer photolithography (MLA150, Heidelberg Instruments) and subjected to a post-baking process (95 °C, 15 min). This is followed by a lift off in SU-8 developer and a crosslinking phase. The fabrication of Au devices follows standard photolithography protocols. For additive manufacturing, CNF solution is first spin coated onto a Si wafer and a pre-designed structure is printed on the substrate with a fused deposition modelling printer (CR-6 SE, Creality). Lift-off experiments for different adhesion layers are conducted by immersing the substrates in hot water (60 °C) without any turbulence.

Device design and fabrication

The serpentine structure and multichannel electrode were designed using AutoCAD software. For the fabrication of multichannel electrodes for sciatic stimulation, a carbon membrane was first produced on paper substrates (Whatman filter paper, Grade 1) using a lasering process. Subsequently, a standard water-phase transfer procedure was applied to transfer the multichannel electrodes onto PET film (12.5 µm). After drying, ~20 µl of Nafion 117 solution (~5% in a mixture of lower aliphatic alcohols and water, Sigma) was applied to the carbon patterns and allowed to dry under ambient conditions for fixation. Multichannel Au electrodes (thickness: Ti, 5 nm; Au, 100 nm) were fabricated using a photomask-based procedure on PET substrate. Devices were rinsed with water and used for biological testing without further pretreatment. To prepare microcapacitor-grafted electrodes for heart modulation, a planar Au film (thickness: Ti, 5 nm; Au, 100 nm) was fabricated on a 50 µm PET substrate via e-beam coating. A serpentine carbon structure was patterned onto a paper substrate and transferred onto the Au electrode using a standard water-phase transfer method. To fabricate carbon-coated recording electrodes, 4 × 4 microelectrode arrays were created on a 25 µm polyimide (PI) film and sealed with PET using a standard photolithography procedure. Carbon was transferred onto the microelectrode array. After drying, a 10 wt% poly(ethylene-vinyl acetate) solution in hexane was applied to the carbon membrane and the assembly was pressed onto the microelectrode array using a commercial hot laminator under a processing temperature of 120 °C.

Material characterization of carbon membrane

The surface structures of various substrates and carbon membranes were characterized using scanning electron microscopy (SEM) (Merlin, Carl Zeiss) at 3 kV. For TEM characterization, carbon samples were separated from substrate, ultrasonicated and dropped onto copper grids (lacey formvar/carbon, Ted Pella). Morphology and crystallinity were observed with a JEM-3010 (JEOL) or a Tecnai F30 (FEI) transmission electron microscope at 300 kV. Scanning transmission electron microscopy (STEM) was performed using a 200-kV aberration-corrected JEOL ARM200F system with a cold field-emission source, providing a spatial resolution of ~0.8 Å. Raman spectra were collected with a LabRAM HR Evolution system (Horiba) using a ×50 objective and a 532 nm laser. Material composition was characterized using X-ray photon spectroscopy (XPS, AXIS Nova, Kratos). X-ray diffraction (XRD) spectra of the paper substrates and carbon membranes were obtained on an XRD spectrometer (MiniFlex, Rigaku) at a wavelength of 1.540593 Å. The surface area and pore size of the carbon membranes were measured with an adsorption analyser (3Flex, Micromeritics).

Ethics oversight
All animal procedures were approved by the Institutional Animal Care and Use Committee of the University of Chicago (protocol number 72378).

In vivo sciatic stimulation
The in vivo stimulation was conducted with cuff-type electrodes interfacing with sciatic nerves[10,45]. Briefly, adult rats (Sprague-Dawley strain, Charles River Laboratories) were deeply anaesthetized with isoflurane (3–4%). The fur was removed from the hindquarters using surgical clippers and hair removal cream. A semi-circular incision across the midline was made on the skin, and the fascial plane was opened between the gluteus maximus and the anterior head of the biceps femoris, thereby exposing the sciatic nerve. Two-electrode configuration was used, where the multichannel device was wrapped around the sciatic nerve. During sciatic stimulation, biphasic waveform was used, with one electrode acting as the working electrode and the other acting as the counter electrode/reference electrode. For EMG recording, stainless-steel needle electrodes in a grounded configuration was inserted into the muscles and connected to an Intantech RHD USB interface board and RHD 16-channel bipolar-input recording headstage. The USB interface board was controlled using RHX software (v.3.0.4, Intantech). The signals were recorded at 10 kS s^{-1} in the 0.1–200 Hz bandwidth. For the analysis of leg displacement, a protractor was placed under the leg as a distance reference. Videos of limb movement were recorded using a digital camera (α6100, Sony).

Electrical heart stimulation ex vivo
Electrical stimulation was conducted with an isolated heart model[34]. Briefly, an adult rat (male, >300 g body weight) was heparinized (1,000 IU kg^{-1} body mass) and anaesthetized with isoflurane. The heart was removed and placed in ice-cold HBSS buffer, and the aorta was cannulated for use in a Langendorff setup. Oxygenated HEPES-buffered Tyrode's solution (pH 7.3) was perfused through the cannulated aorta after a heating coil and bubble trap to maintain a temperature of 37 °C. The sinoatrial node along with the atria was removed to lower the atrioventricular node pace. The perfusion pressure was monitored using a BP-100 probe (iWorx) connected to the perfusion line and was maintained at 80–100 mmHg. Left ventricular pressure was monitored through a water-filled balloon (Radnoti) inserted into the left ventricle. For ECG recordings, needle electrodes were positioned on the left ventricular wall and aorta, grounded on the cannula and connected to a C-ISO-256 preamplifier (iWorx). All signals (perfusion, left ventricular pressure and ECG) were amplified using an IA-400D amplifier (iWorx) and interfaced with a computer using a Digidata 1550 digitizer with Clampex software (v.10.7, Molecular Devices).

Stimulation electrodes (0.5 cm × 0.5 cm) were connected in a two-electrode configuration, where the working electrode was placed on the left ventricular wall, while the counter electrode was placed on the right ventricular wall and connected to the ground. Square current waveforms were delivered through a potentiostation (SP-200, BioLogic), and the potential between the two electrodes was recorded during stimulation.

Electrical recording was performed using a 4 × 4 microelectrode array (2 mm spacing between electrodes) and recorded using an Intantech RHD USB interface board and RHD 16-channel input recording headstage. The signals were recorded at 10 kS s^{-1} in the 0.1–100 Hz bandwidth. Isochrone maps of the electrical propagation were calculated using Python. A timestamp of peak positive signal deflection for each contraction was determined and the average was calculated for multiple signals. Gaussian interpolation was used for map rendering to improve readability.

Biomimetic Hg(II) detection using catalytic robotics
Water strider-like robots were fabricated using a lasering process after Pt-incorporated salt impregnation and transferred onto PET substrates (12.5 μm). Nafion 117 was employed to secure the functional carbon on the supporting substrates. Motion behaviours of robots in polytetrafluoroethylene containers were recorded using a digital camera (α6100, Sony). Recorded videos were processed using the DeepLabCut toolbox[38], a markerless pose tracking algorithm based on deep neural network training. Videos were initially segmented and extracted into batches of 50 images per video using *k*-means algorithm. Centre point positions were manually labelled and subsequently used for training the neural network model on the basis of the ResNet50 framework with an iteration of 5,000 epochs. Predicted positions were evaluated using a validation set to determine the maximum error in axial coordinates in terms of pixels. Once trained, the neural network was utilized to apply labels to new videos for batch processing.

Buildup of R2R apparatus
A roll-to-roll apparatus was designed using Autodesk Inventor, with mechanical components and raw materials sourced from McMaster-Carr. The machining and assembly took place in-house at the University of Chicago MRSEC Student Machine Shop. During the assembly process, paper was fed from the supply roll (width of 6 cm) through a set of idler rollers and pulled using a capstan roll driven by a stepper motor. A Joule heater was assembled from resistive wire and enclosed in high-temperature fibreglass electrical insulation sleeving. The heater was powered by a benchtop AC–AC converter (operation voltage of 15 V) connected to the standard North American 110 VAC electrical grid. A refurbished K40 CO_2 laser was controlled by Python scripts and coordinated with a stepper motor integrated into an Arduino board. The control software was based on the K40 Whisperer source code, which was obtained from https://www.scorchworks.com/K40whisperer/k40whisperer.html#download and distributed under the GNU General Public License. The software was modified to allow control of the roller stepper motor and execute sequential pre-programmed ablation. The detailed design of the R2R system can be found in Extended Data Fig. 3.

Life cycle analysis
In our study, we conducted a cradle-to-gate LCA to analyse the environmental impacts arising from the production of devices using both conventional methods (CVD, pyrolysis, lasering) and our approach[46,47]. This evaluation aims to quantify the total environmental impacts and the contribution from each fabrication process. The system boundary includes the extraction and processing of raw materials, energy consumption and waste generation, specifically excluding the product's usage, end-of-life disposal and the construction of utilities[8]. The functional unit was defined as 1 m^2 of monolithic device. Life cycle inventory data for each method were organized according to standard laboratory practices within the established system boundary (Extended Data Fig. 4). The LCA was performed using the Ecoinvent database (v.3.8) in SimaPro (v.9.4)[48]. The TRACI 2.1 (v.1.07/US 2008) method was employed for the assessment of total GHG emissions and other environmental impacts[49,50].

Data processing and statistics
Analysis of numerical data and plotting was performed using OriginLab (v.2021), Microsoft Excel (v.2016), Python (v.3.8.12) scripts using NumPy (v.1.22.1), Matplotlib (v.3.5.1), Scipy (v.1.7.3), pybaselines (v.0.8.0) and Seaborn (v.0.11.2) libraries. Machine learning-based video processing was analysed with DeepLabCut (v.2.3) under the CONDA environment. Data were statistically analysed using ordinary one-way analysis of variance comparisons test with GraphPad Prism (v.9), unless specified in the figure legends. Electron microscopy images were processed using ImageJ (Fiji, v.1.53t). Adobe Premiere 2021 was used for cropping and slicing video recordings. The recordings from the 16-channel device on the ex vivo rat heart were analysed using customized Python scripts.

Reporting summary
Further information on research design is available in the Nature Portfolio Reporting Summary linked to this article.

Data availability
The research findings presented in this study are supported by data included in the main text and in Supplementary Information. Source data are provided with this paper and are publicly available at https://osf.io/zfqhk/.

Code availability
Scripts used for data analysis and R2R operation in this study can be accessed from https://osf.io/zfqhk/.

References

1. Park, S. et al. Self-powered ultra-flexible electronics via nano-grating-patterned organic photovoltaics. *Nature* **561**, 516–521 (2018).
2. Hwangbo, S., Hu, L., Hoang, A. T., Choi, J. Y. & Ahn, J.-H. Wafer-scale monolithic integration of full-colour micro-LED display using MoS2 transistor. *Nat. Nanotechnol.* **17**, 500–506 (2022).
3. Wang, Q. et al. Environmental data and facts in the semiconductor manufacturing industry: an unexpected high water and energy consumption situation. *Water Cycle* **4**, 47–54 (2023).
4. Xia, Y. & Whitesides, G. M. Soft lithography. *Annu. Rev. Mater. Sci.* **28**, 153–184 (1998).
5. Chang, Y. et al. Closed-loop electrochemical recycling of spent copper(II) from etchant wastewater using a carbon nanotube modified graphite felt anode. *Environ. Sci. Technol.* **52**, 5940–5948 (2018).
6. *Global Etching Chemicals Market 2023–2032* (Custom Market Insights, 2023).
7. Branham, M. S. & Gutowski, T. G. Deconstructing energy use in microelectronics manufacturing: an experimental case study of a MEMS fabrication facility. *Environ. Sci. Technol.* **44**, 4295–4301 (2010).
8. Murphy, C. F., Kenig, G. A., Allen, D. T., Laurent, J.-P. & Dyer, D. E. Development of parametric material, energy, and emission inventories for wafer fabrication in the semiconductor industry. *Environ. Sci. Technol.* **37**, 5373–5382 (2003).
9. Bae, S. et al. Roll-to-roll production of 30-inch graphene films for transparent electrodes. *Nat. Nanotechnol.* **5**, 574–578 (2010).
10. Fang, Y. et al. Micelle-enabled self-assembly of porous and monolithic carbon membranes for bioelectronic interfaces. *Nat. Nanotechnol.* **16**, 206–213 (2021).
11. Bubnova, O. A decade of R2R graphene manufacturing. *Nat. Nanotechnol.* **16**, 1050 (2021).
12. Sviben, S. et al. Epidermal cell surface structure and chitin–protein co-assembly determine fiber architecture in the locust cuticle. *ACS Appl. Mater. Interfaces* **12**, 25581–25590 (2020).
13. Qu, L., Dai, L., Stone, M., Xia, Z. & Wang, Z. L. Carbon nanotube arrays with strong shear binding-on and easy normal lifting-off. *Science* **322**, 238–242 (2008).
14. Fraley, S. I. et al. A distinctive role for focal adhesion proteins in three-dimensional cell motility. *Nat. Cell Biol.* **12**, 598–604 (2010).
15. Khare, E., Holten-Andersen, N. & Buehler, M. J. Transition-metal coordinate bonds for bioinspired macromolecules with tunable mechanical properties. *Nat. Rev. Mat.* **6**, 421–436 (2021).
16. Lin, J. et al. Laser-induced porous graphene films from commercial polymers. *Nat. Commun.* **5**, 5714–2721 (2014).
17. Luong, D. X. et al. Gram-scale bottom-up flash graphene synthesis. *Nature* **577**, 647–651 (2020).
18. Baban, N. S., Orozaliev, A., Kirchhof, S., Stubbs, C. J. & Song, Y.-A. Biomimetic fracture model of lizard tail autotomy. *Science* **375**, 770–774 (2022).
19. Nakamura, T., Takashima, Y., Hashidzume, A., Yamaguchi, H. & Harada, A. A metal–ion-responsive adhesive material via switching of molecular recognition properties. *Nat. Commun.* **5**, 4622–4630 (2014).
20. Baxamusa, S. H. et al. Enhanced delamination of ultrathin free-standing polymer films via self-limiting surface modification. *Langmuir* **30**, 5126–5132 (2014).
21. Freund, L. B. & Suresh, S. *Thin Film Materials: Stress, Defect Formation and Surface Evolution* (Cambridge Univ. Press, 2004).
22. Zhuk, A. V., Evans, A. G., Hutchinson, J. W. & Whitesides, G. M. The adhesion energy between polymer thin films and self-assembled monolayers. *J. Mater. Res.* **13**, 3555–3564 (1998).
23. Ma, J. et al. Role of thin film adhesion on capillary peeling. *Nano Lett.* **21**, 9983–9989 (2021).
24. Hu, Z. et al. Rapid and scalable transfer of large-area graphene wafers. *Adv. Mater.* **35**, e2300621 (2023).
25. Gao, L. et al. Repeated growth and bubbling transfer of graphene with millimetre-size single-crystal grains using platinum. *Nat. Commun.* **3**, 699–705 (2012).
26. Leong, W. S. et al. Paraffin-enabled graphene transfer. *Nat. Commun.* **10**, 867 (2019).
27. Zhao, Y. et al. Large-area transfer of two-dimensional materials free of cracks, contamination and wrinkles via controllable conformal contact. *Nat. Commun.* **13**, 4409 (2022).
28. Gao, L. et al. Face-to-face transfer of wafer-scale graphene films. *Nature* **505**, 190–194 (2014).
29. Wang, M. et al. Single-crystal, large-area, fold-free monolayer graphene. *Nature* **596**, 519–524 (2021).
30. Li, J. et al. A tissue-like neurotransmitter sensor for the brain and gut. *Nature* **606**, 94–101 (2022).
31. Li, T. et al. Denary oxide nanoparticles as highly stable catalysts for methane combustion. *Nat. Catal.* **4**, 62–70 (2021).
32. Pinheiro, T. et al. Water peel-off transfer of electronically enhanced, paper-based laser-induced graphene for wearable electronics. *ACS Nano* **16**, 20633–20646 (2022).
33. Nair, V. et al. Laser writing of nitrogen-doped silicon carbide for biological modulation. *Sci. Adv.* **6**, eaaz2743 (2020).
34. Prominski, A. et al. Porosity-based heterojunctions enable leadless optoelectronic modulation of tissues. *Nat. Mater.* **21**, 647–655 (2022).
35. Merrill, D. R. in *Implantable Neural Prostheses 2: Techniques and Engineering Approaches* (eds Zhou, D. & Greenbaum, E.) 85–138 (Springer, 2010).
36. Zeng, M. et al. Printing thermoelectric inks toward next-generation energy and thermal devices. *Chem. Soc. Rev.* **51**, 485–512 (2022).
37. Kay, G. N. & Shepard, R. B. in *Clinical Cardiac Pacing, Defibrillation, and Resynchronization Therapy* 5th edn (eds Ellenbogen, K. A. et al.) 61–113 (Elsevier, 2017).
38. Nath, T. et al. Using DeepLabCut for 3D markerless pose estimation across species and behaviors. *Nat. Protoc.* **14**, 2152–2176 (2019).
39. Yu, Y. et al. All-printed soft human-machine interface for robotic physicochemical sensing. *Sci. Robot.* **7**, eabn0495 (2022).
40. Huang, H. et al. Large-scale self-assembly of MOFs colloidosomes for bubble-propelled micromotors and stirring-free environmental remediation. *Angew. Chem. Int. Ed.* **61**, e202211163 (2022).
41. Li, W. et al. Self-driven magnetorobots for recyclable and scalable micro/nanoplastic removal from nonmarine waters. *Sci. Adv.* **8**, eade1731 (2022).

42. Urso, M., Ussia, M. & Pumera, M. Smart micro- and nanorobots for water purification. *Nat. Rev. Bioeng.* **1**, 236–251 (2023).
43. Ullah, S. et al. Graphene transfer methods: a review. *Nano Res.* **14**, 3756–3772 (2021).
44. Li, S.-C. et al. Wood-derived ultrathin carbon nanofiber aerogels. *Angew. Chem. Int. Ed. Engl.* **57**, 7085–7090 (2018).
45. Kim, D.-H. et al. Dissolvable films of silk fibroin for ultrathin conformal bio-integrated electronics. *Nat. Mater.* **9**, 511–517 (2010).
46. Frischknecht, R. et al. *Implementation of Life Cycle Impact Assessment Methods* Ecoinvent Report No. 3 (Swiss Centre for Life Cycle Inventories, 2007).
47. Finkbeiner, M., Inaba, A., Tan, R., Christiansen, K. & Klüppel, H.-J. The new international standards for life cycle assessment: ISO 14040 and ISO 14044. *Int. J. Life Cycle Assess.* **11**, 80–85 (2006).
48. Wernet, G. et al. The ecoinvent database version 3 (part I): overview and methodology. *Int. J. Life Cycle Assess.* **21**, 1218–1230 (2016).
49. Bare, J. TRACI 2.0: the tool for the reduction and assessment of chemical and other environmental impacts 2.0. *Clean. Technol. Environ. Policy* **13**, 687–696 (2011).
50. Bare, J. C. TRACI: the tool for the reduction and assessment of chemical and other environmental impacts. *J. Ind. Ecol.* **6**, 49–78 (2002).

Acknowledgements

We thank K. M. Watters for scientific editing of the paper. This work was supported by the US Air Force Office of Scientific Research (FA9550-20-1-0387), the National Science Foundation (NSF CBET-2128140, NSF MPS-2121044) and the US Army Research Office (W911NF-21-1-0090). L.J. and C.W. acknowledge the support of the National Science Foundation (NSF CMMI-1925790). This work made use of the shared facilities at the University of Chicago Materials Research Science and Engineering Center, supported by the National Science Foundation under award number DMR-2011854. Parts of this work were carried out at the Soft Matter Characterization Facility of the University of Chicago. We acknowledge the Pritzker Nanofabrication Facility at the Pritzker School of Molecular Engineering of the University of Chicago, which receives support from the Soft and Hybrid Nanotechnology Experimental (SHyNE) Resource (NSF ECCS-2025633), a node of the National Science Foundation's National Nanotechnology Coordinated Infrastructure. This work used instruments at the Electron Microscopy Core (Research Resources Center, UIC). We acknowledge the support of J. Jureller and S. Brown in spectral collection and materials characterization. Parts of the diagrams in Figs. 1j, 3a, 3d, and 5c were created with BioRender.com.

Author contributions

B.T. and L.J. supervised the research. C.Y. and B.T. conceived the idea and designed the experiments. C.Y. conducted most of the experiments and data analysis. P.L. assisted with the bioelectronics fabrication, cardiac recording and experiment designs. Theoretical simulations were performed by C.W. and L.J. A.P. and C.Y. constructed the R2R device. J.Z. and J.Y. assisted with the in vitro heart and in vivo sciatic nerve experiments. C.S. and Z.C. contributed to the fabrication experiments. W.L. and P.G. helped with the Brunauer–Emmett–Teller (BET) measurements. J.S. assisted with the hot compression experiments. F.S. supported the STEM and HRTEM experiments. Data analysis and processing were collaboratively performed by C.Y., C.W., P.L., C.S., B.A., K.H. and J.M. The paper was prepared by C.Y., C.W., L.J. and B.T., with input from all other authors.

Competing interests

The University of Chicago filed provisional patent applications for the permeable junction-based synthesis platform for carbon-based bioelectronics and robotics in Chicago, 2024. B.T., C.Y. and P.L. are the inventors. The other authors declare no competing interests.

Additional information

Extended data is available for this paper at https://doi.org/10.1038/s41893-024-01389-5.

Supplementary information The online version contains supplementary material available at https://doi.org/10.1038/s41893-024-01389-5.

Correspondence and requests for materials should be addressed to Chuanwang Yang, Lihua Jin or Bozhi Tian.

Peer review information *Nature Sustainability* thanks Levent Beker, Jing Meng and the other, anonymous, reviewer(s) for their contribution to the peer review of this work.

https://doi.org/10.1038/s41893-024-01389-5

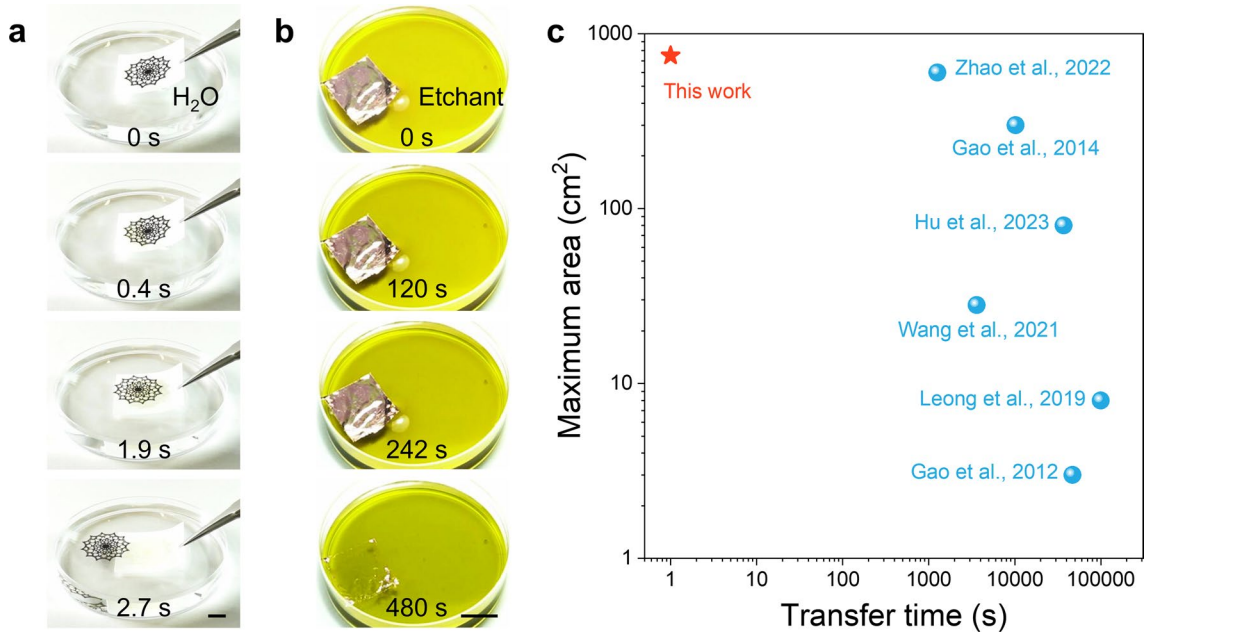

Extended Data Fig. 1 | Comparison of our transfer technique with other graphene transfer methods. (**a**) Image sequences showing the instantaneous delamination of carbon pattern from a paper substrate in water. Scale bar, 1 cm. (**b**) Image sequences showing the release of polymethyl methacrylate-coated graphene layer from Cu foil in etchant. Scale bar, 1 cm. (**c**) Comparison of different transfer techniques in terms of transfer time and the maximum area in our work and previous works.

https://doi.org/10.1038/s41893-024-01389-5

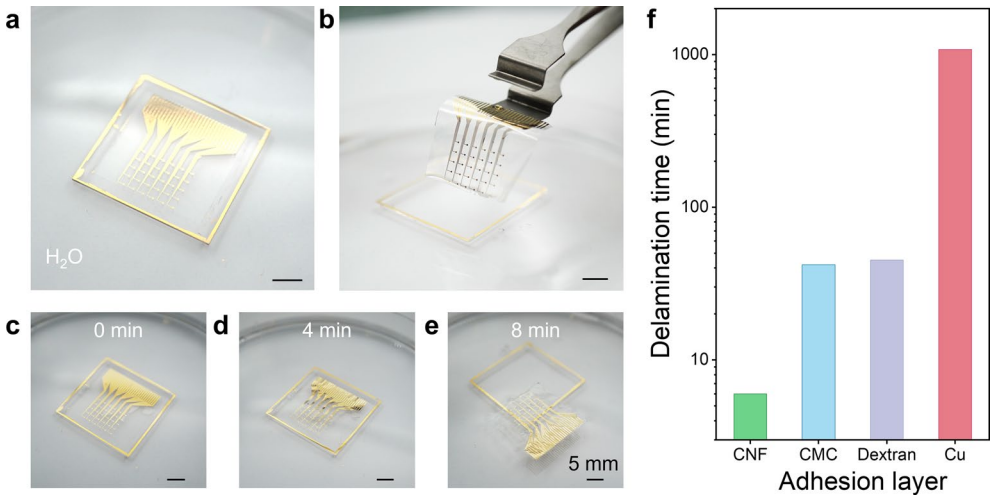

Extended Data Fig. 2 | Permeable nanojunction-facilitated fast release of microfabricated devices on rigid substrate. (**a-b**) Optical images of the multichannel device before and after release from a glass slide. Scale bar, 5 mm. Image (a) shows the device attached to the substrate with CNF as the adhesion layer, whereas image (b) reveals it post-release in H_2O. (**c-e**) Image sequences showing the release process in water at 60 °C at 0, 4, and 8 min. The device has completely separated from the glass substrate after 8 min. Scale bar, 5 mm. (**f**) A comparative analysis of the time required for complete delamination with each type of adhesion layer.

https://doi.org/10.1038/s41893-024-01389-5

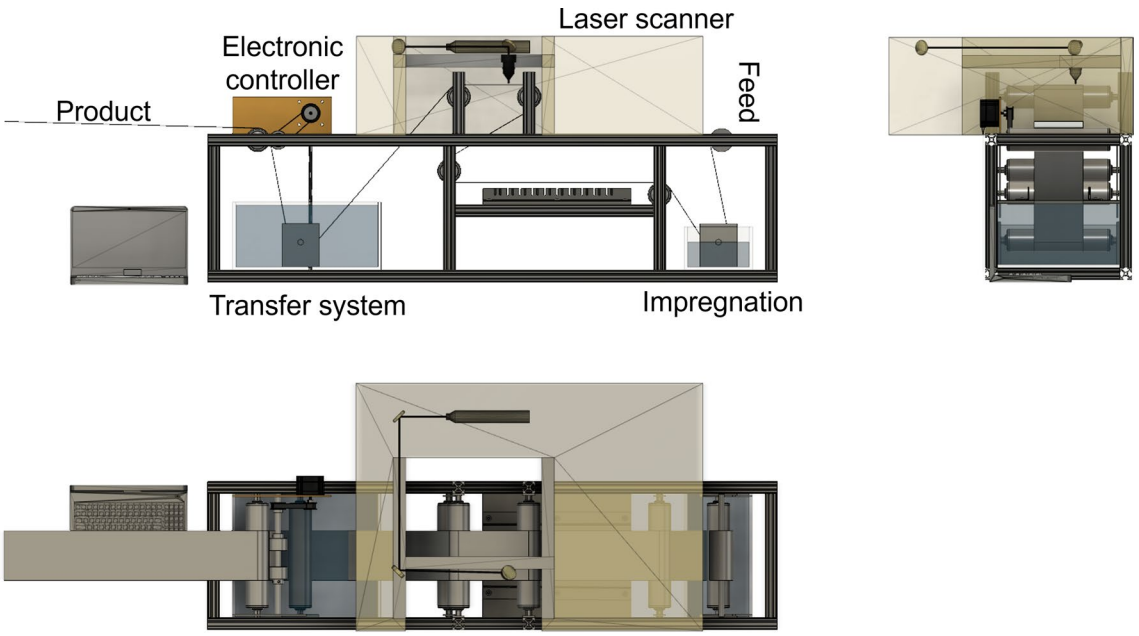

Extended Data Fig. 3 | 3D illustration of the home-built R2R apparatus. Front, side, and top views illustrating the components of the R2R apparatus, including the paper feed system, laser scanner, roller system, salt-impregnation system, electronic controller, product, and transfer system.

https://doi.org/10.1038/s41893-024-01389-5

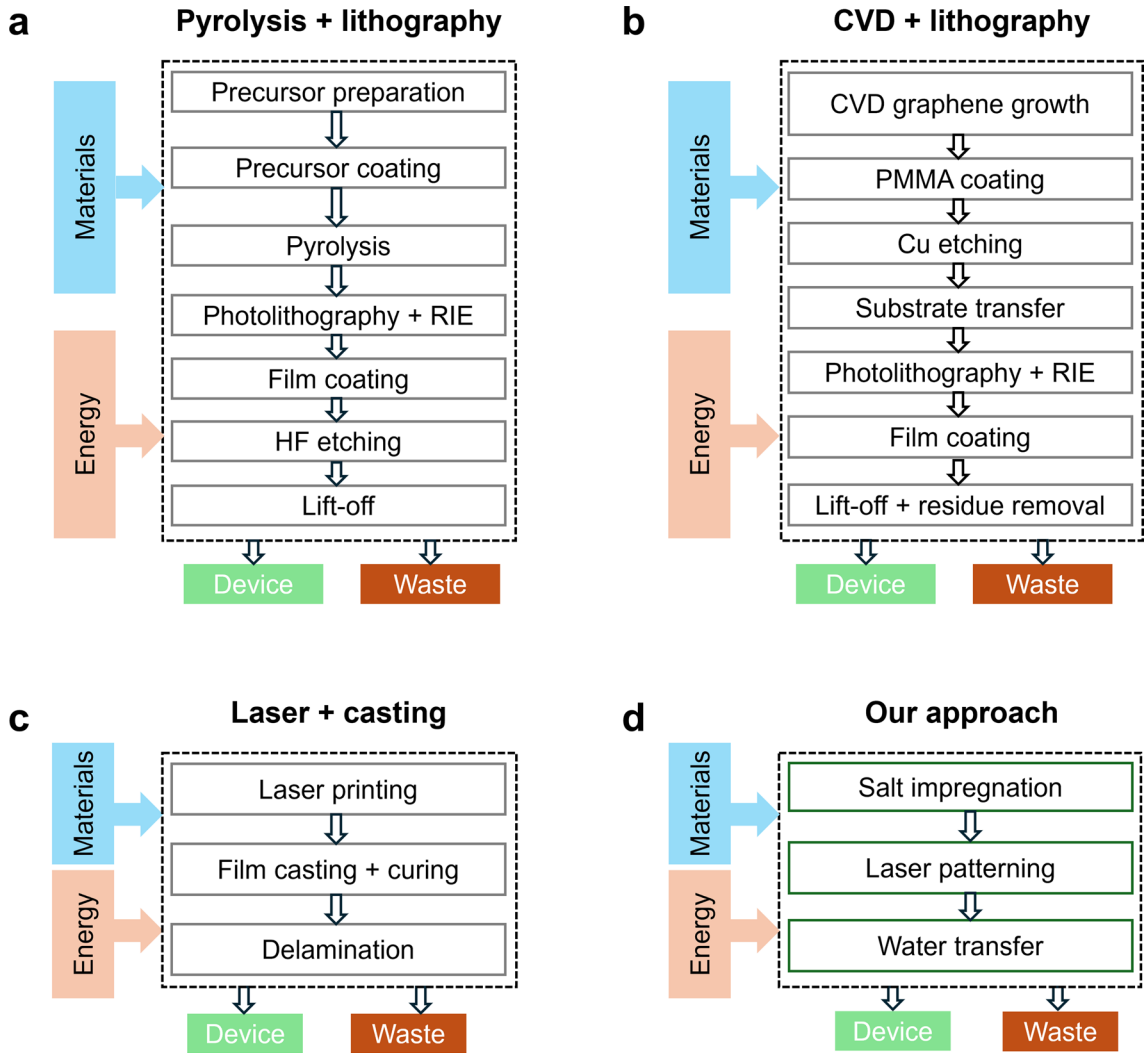

Extended Data Fig. 4 | System boundaries of device fabrication through four fabrication routes. (**a**) Pyrolysis + lithography route, (**b**) CVD + lithography route, (**c**) lasering + casting route, and (**d**) the approach described in this study.

https://doi.org/10.1038/s41893-024-01389-5

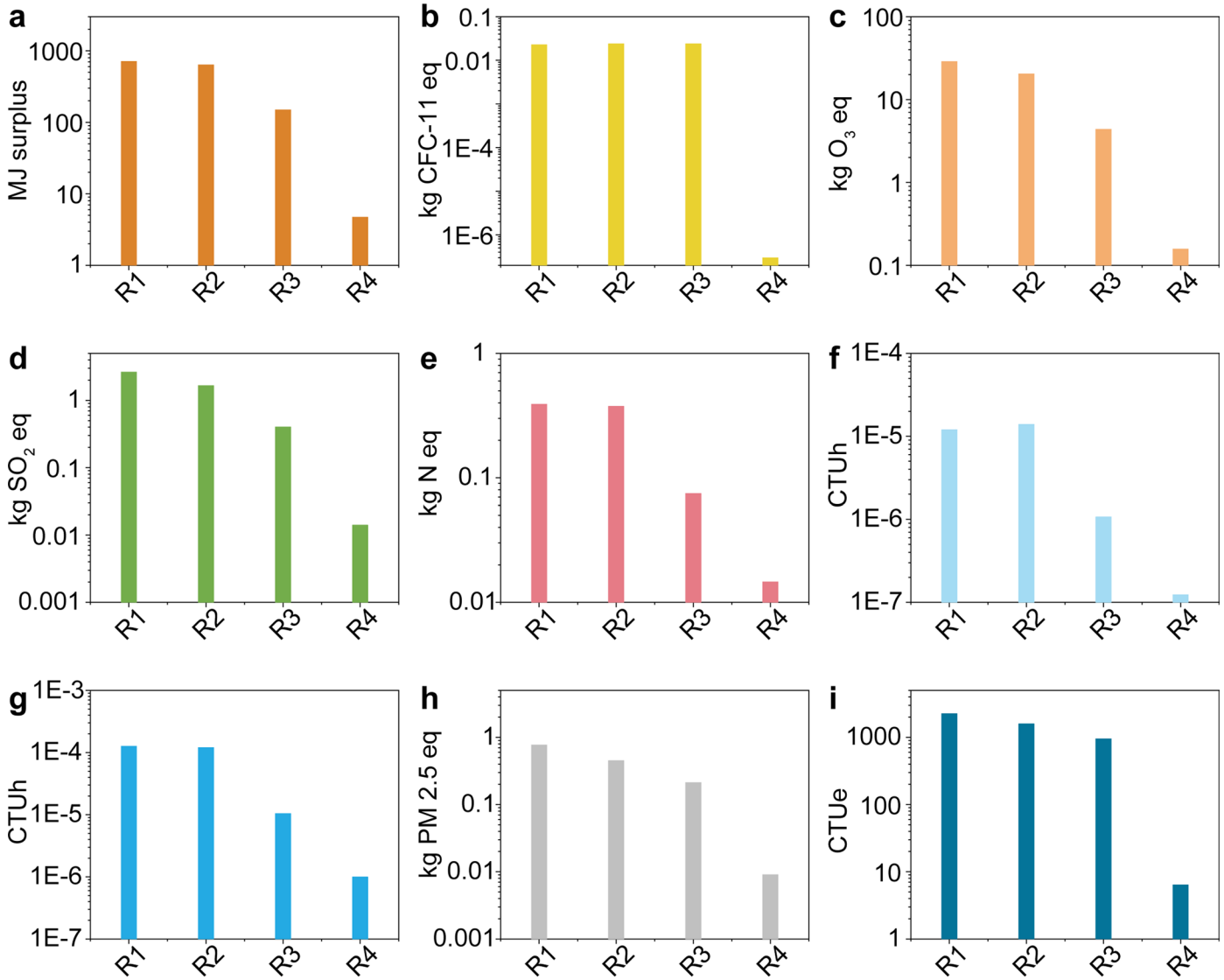

Extended Data Fig. 5 | Comparative analysis of environmental impacts for device fabrication through four routes. The environmental impact per functional unit is quantified across nine categories: (**a**) Fossil fuel depletion (measured in MJ surplus), (**b**) Ozone depletion (measured in kg CFC-11 eq), (**c**) Smog (measured in kg O_3 eq), (**d**) Acidification (measured in kg SO_2 eq), (**e**) Eutrophication (measured in kg N eq), (**f**) Carcinogenic effects (measured in CTUh), (**g**) Noncarcinogenic effects (measured in CTUh), (**h**) Respiratory effects (measured in kg $PM_{2.5}$ eq), and (**i**) Ecotoxicity (measured in CTUe).

nature portfolio

Corresponding author(s): Bozhi Tian, Lihua Jin, Chuanwang Yang

Last updated by author(s): Jun 2, 2024

Reporting Summary

Nature Portfolio wishes to improve the reproducibility of the work that we publish. This form provides structure for consistency and transparency in reporting. For further information on Nature Portfolio policies, see our Editorial Policies and the Editorial Policy Checklist.

Statistics

For all statistical analyses, confirm that the following items are present in the figure legend, table legend, main text, or Methods section.

n/a	Confirmed
☐	☒ The exact sample size (*n*) for each experimental group/condition, given as a discrete number and unit of measurement
☐	☒ A statement on whether measurements were taken from distinct samples or whether the same sample was measured repeatedly
☐	☒ The statistical test(s) used AND whether they are one- or two-sided *Only common tests should be described solely by name; describe more complex techniques in the Methods section.*
☐	☒ A description of all covariates tested
☐	☒ A description of any assumptions or corrections, such as tests of normality and adjustment for multiple comparisons
☐	☒ A full description of the statistical parameters including central tendency (e.g. means) or other basic estimates (e.g. regression coefficient) AND variation (e.g. standard deviation) or associated estimates of uncertainty (e.g. confidence intervals)
☐	☒ For null hypothesis testing, the test statistic (e.g. *F*, *t*, *r*) with confidence intervals, effect sizes, degrees of freedom and *P* value noted *Give P values as exact values whenever suitable.*
☒	☐ For Bayesian analysis, information on the choice of priors and Markov chain Monte Carlo settings
☒	☐ For hierarchical and complex designs, identification of the appropriate level for tests and full reporting of outcomes
☒	☐ Estimates of effect sizes (e.g. Cohen's *d*, Pearson's *r*), indicating how they were calculated

Our web collection on statistics for biologists contains articles on many of the points above.

Software and code

Policy information about availability of computer code

Data collection	No unique software was used to perform data collection and manufacture software was generally used. Theoretical simulation was analyzed using ABAQUS (v. 2020) with cohesive zone model. Laser writer was controlled with Universal Control Panel (v. 4.60). Potentiostat (SP-200, BioLogic) was controlled using EC-Lab software (v. 1.33, BioLogic). Fergie spectrometer was controlled using LightField software (v. 6.1, Princeton Instruments). Intantech RHD USB interface board was controlled using RHX software (v. 3.0.4, Intantech). IA-400D amplifier (iWorx) is interfaced with a computer using a Digidata 1550 digitizer with Clampex software (v. 10.7, Molecular Devices). The control software of R2R apparatus was based on the K40 Whisperer source code, which was obtained from https://www.scorchworks.com/K40whisperer/k40whisperer.html#download and distributed under the GNU GPL. The LCA was performed using the Ecoinvent database (version 3.8) in SimaPro software (version 9.4).
Data analysis	Analysis of numerical data and plotting was performed with OriginLab (v. 2021), Microsoft Excel (v. 2016), Python (v. 3.8.12) scripts using NumPy (v. 1.22.1), Matplotlib (v. 3.5.1), Scipy (v.1.7.3), pybaselines (v. 0.8.0) and Seaborn (v. 0.11.2) libraries. Machine learning-based video processing was analyzed with DeepLabCut (v. 2.3) under CONDA environment. Data were statistically analyzed with ordinary one-way analysis of variance comparisons test with Prism (v. 9, GraphPad) unless specified in the figure legends. Electron microscopy images were processed using ImageJ (Fiji, v. 1.53t). Adobe Premiere 2021 was used for cropping and slicing video recordings. The recordings from the 16-channel device on the ex vivo rat heart were analysed by customized Python scripts.

For manuscripts utilizing custom algorithms or software that are central to the research but not yet described in published literature, software must be made available to editors and reviewers. We strongly encourage code deposition in a community repository (e.g. GitHub). See the Nature Portfolio guidelines for submitting code & software for further information.

Data

Policy information about availability of data

All manuscripts must include a data availability statement. This statement should provide the following information, where applicable:

- Accession codes, unique identifiers, or web links for publicly available datasets
- A description of any restrictions on data availability
- For clinical datasets or third party data, please ensure that the statement adheres to our policy

The research findings presented in this study are supported by data included in the main text and Supplementary Information. The source data and codes are provided with this paper, and publicly available at https://osf.io/zfqhk/.

Human research participants

Policy information about studies involving human research participants and Sex and Gender in Research.

Reporting on sex and gender	not applicable
Population characteristics	not applicable
Recruitment	not applicable
Ethics oversight	not applicable

Note that full information on the approval of the study protocol must also be provided in the manuscript.

Field-specific reporting

Please select the one below that is the best fit for your research. If you are not sure, read the appropriate sections before making your selection.

☒ Life sciences ☐ Behavioural & social sciences ☐ Ecological, evolutionary & environmental sciences

For a reference copy of the document with all sections, see nature.com/documents/nr-reporting-summary-flat.pdf

Life sciences study design

All studies must disclose on these points even when the disclosure is negative.

Sample size	For material preparation and characterization, a sample size of N≥3 was selected in both material preparation and testing procedures. Specifically, for the swelling experiment (Figure 2e), the sample sizes were N=7 for the 0%, 25%, 50%, and 100% groups, and N=5 for the 75% group. For the chelating experiment (Figure 2f), the sample sizes were N=8 for Ctrl, N=6 for Fe(III), N=6 for Co(III), N=7 for Cu(II), N=6 for Zn(II), N=7 for Fe-EDTA, N=6 for Co-EDTA, N=7 for Cu-EDTA, and N=6 for Zn-EDTA. The sample size number was N=3 for wicking experiment (Figure 2h). The biological sample size for animal stimulation experiments was N=3. During animal stimulation, the number of devices were N=4 for heart stimulation, and N=6 for sciatic stimulation. The sample size was N=3 for bubble growth dynamics experiment (Figure 5e). During robotic sensing and remediation, a individual sample set underwent testing for demonstrative purposes, yielding an excess of 100 data points in the motion tracking segment. For Figure 6e, the data was derived from n=1,000 trials of Monte Carlo simulation within 95% confidence interval.
Data exclusions	Representative images of experiments are shown in manuscript and SI.
Replication	All experimental outcomes, encompassing material fabrication, scanning electron microscopy (SEM) images, scanning tunneling microscopy (STM) mapping, micro-computed tomography (Micro-CT) images, microscopic visualizations, Raman spectra, X-ray diffraction (XRD) spectra, Fourier-transform infrared spectroscopy (FTIR), water release experiments, biological stimulation, and robotic sensing, demonstrated robust reproducibility. For the material fabrication and characterization dimensions, a minimum of 3 replicates were utilized in each experimental set. In the realm of animal stimulation experiments, no fewer than 4 devices were tested on animal models for comparative analysis.
Randomization	No randomization was conducted in the study. The investigation focused solely on the impact of electrical pulse stimulation, for which no known covariates exist. Subjects for the experiment were selected from a uniform population of laboratory rats. Each rat served as the subject for multiple devices, minimizing the potential for inter-subject variability. Given the homogeneous subject pool and the single-factor experimental design, we anticipate minimal variability in response to electrical stimulation throughout the duration of the experiment.
Blinding	The entirety of the material preparation and animal experiments was executed by the lead author, precluding the availability of additional personnel to conduct blinded investigations. In terms of material characterization, the assessments adhered to standardized protocols, rendering the absence of experiment blinding inconsequential to the introduction of bias in the results.

Reporting for specific materials, systems and methods

We require information from authors about some types of materials, experimental systems and methods used in many studies. Here, indicate whether each material, system or method listed is relevant to your study. If you are not sure if a list item applies to your research, read the appropriate section before selecting a response.

Materials & experimental systems

n/a	Involved in the study
☒	☐ Antibodies
☒	☐ Eukaryotic cell lines
☒	☐ Palaeontology and archaeology
☐	☒ Animals and other organisms
☒	☐ Clinical data
☒	☐ Dual use research of concern

Methods

n/a	Involved in the study
☒	☐ ChIP-seq
☒	☐ Flow cytometry
☒	☐ MRI-based neuroimaging

Animals and other research organisms

Policy information about studies involving animals; ARRIVE guidelines recommended for reporting animal research, and Sex and Gender in Research

Laboratory animals	Adult rats (strain, Sprague-Dawley), both female and male, aged between 10 and 16 weeks and weighing approximately 300 grams, were initially sourced from Charles River Laboratories. These rats were subsequently housed and bred in the University of Chicago's animal facility. Utilized as heart donors in ex vivo isolated heart experiments, these animals also served as subjects in in vivo studies focusing on sciatic nerve stimulation.
Wild animals	No wild animals were used in this study.
Reporting on sex	No sex information were collected in this study.
Field-collected samples	No field-collected samples were used in this study.
Ethics oversight	All animal procedures were approved by the Institutional Animal Care and Use Committee of the University of Chicago in the protocol number 72378.

Note that full information on the approval of the study protocol must also be provided in the manuscript.